

## Impacts of the Diurnal Radiation Cycle on the Formation, Intensity, and Structure of Hurricane Edouard (2014)

XIAODONG TANG

*Key Laboratory of Mesoscale Severe Weather, Ministry of Education, and School of Atmospheric Sciences, Nanjing University, Nanjing, China, and Department of Meteorology, and Center for Advanced Data Assimilation and Predictability Techniques, The Pennsylvania State University, University Park, Pennsylvania*

FUQING ZHANG

*Department of Meteorology, and Center for Advanced Data Assimilation and Predictability Techniques, The Pennsylvania State University, University Park, Pennsylvania*

(Manuscript received 18 September 2015, in final form 16 March 2016)

### ABSTRACT

This work examines the impacts of the diurnally varying radiation cycle on the formation, intensity, structure, and track of Hurricane Edouard (2014) at different stages of its life cycle through convection-permitting simulations. During the formation stage, nighttime destabilization through radiative cooling may promote deep moist convection that eventually leads to the genesis of the storm, while a tropical cyclone fails to develop in the absence of the night phase despite a strong incipient vortex under moderately strong vertical wind shear. The nighttime radiative cooling further enhances the primary vortex before the storm undergoes rapid intensification. Thereafter, the nighttime radiative cooling mainly increases convective activities outside of the primary eyewall that lead to stronger/broader rainbands and larger storm size during the mature stage of the hurricane; there is, however, less impact on the hurricane's peak intensity in terms of maximum 10-m surface wind speed. The control forecast undergoes distinct secondary eyewall formation during the mature stage of Edouard (as observed), while there is no apparent eyewall replacement cycle as simulated in sensitivity experiments without solar insolation and the moat is narrower in those with switch-on solar insolation at night, suggesting the potential role of the diurnally varying radiative impact.

### 1. Introduction

A significant diurnal cycle of tropical convection and tropical cyclone (TC) cirrus canopy has been described extensively in numerous studies using satellite imagery (Browner et al. 1977; Muramatsu 1983; Lajoie and Butterworth 1984; Steranka et al. 1984; Kossin 2002; Dunion et al. 2014). Some studies (e.g., Dunion et al. 2014) speculate that the TC diurnal cycle might influence the TC intensity and structure changes. A recent climatological study of Yaroshevich and Ingel (2013)

showed that TCs in the northwestern tropical Pacific, on average, intensify (decay) much faster (slower) at night. Satellite-derived observations also indicated apparent diurnal oscillations of precipitation associated with TCs (Browner et al. 1977; Shu et al. 2013; Wu et al. 2015).

The TC diurnal cycle may be ultimately attributed to the diurnal variation of radiative forcing. Three leading mechanisms have been proposed in explaining the effects of radiation on deep moist convection: 1) change in convective instability due to radiation difference between the cloud top and cloud base (Webster and Stephens 1980; Hobgood 1986; Xu and Randall 1995), 2) differential heating between deep cumulus convection and the surrounding cloud-free region (Gray and Jacobson 1977; Craig 1996), and 3) large-scale nighttime environment cooling (Dudhia 1989; Tao et al. 1996; Johnson et al. 1999; Melhauser and Zhang 2014). The first mechanism is attributed to being the primary cause of TC diurnal oscillation by Hobgood (1986): net

---

 Denotes Open Access content.

---

*Corresponding author address:* Xiaodong Tang, Ph.D., School of Atmospheric Sciences, Nanjing University, 163 Xianlin Avenue, Nanjing 210023, China.  
E-mail: xdtang@nju.edu.cn

DOI: 10.1175/JAS-D-15-0283.1

cloud-top cooling at night steepens the lapse rate, thus promoting convection while the daytime absorption of solar radiation at cloud tops reverses this process. Hobgood also suggested this process might be augmented by the second mechanism. The second mechanism on differential heating between convective and cloud-free regions was found in [Craig \(1996\)](#) to be solely responsible for the enhancement of the diurnal variation in the TC growth rate and intensity, using an axisymmetric model with explicit convection. The third mechanism could result in nighttime destabilization of the local and large-scale environment through radiative cooling, promoting deep moist convection and increasing the TC genesis potential ([Melhauser and Zhang 2014](#)). While these early modeling studies provided strong evidence of TC diurnal variation, the rather simplistic resolution and physics including cloud and radiation schemes these models used might have been a strong limiting factor toward a full understanding of the impacts and mechanisms of the TC diurnal cycle.

The impact of the diurnal radiation cycle on the genesis of TC has recently been studied in a real-case modeling ([Melhauser and Zhang 2014](#)) and in idealized simulations ([Nicholls 2015](#)) with state-of-the-art high-resolution convection-permitting simulations that include sophisticated cloud and microphysics schemes. Both studies suggested that radiative forcing causes accelerated rates of tropical cyclogenesis during the TC formation stage, though they differed in what was attributed to being the primary mechanism in leading these diurnal variations and impacts. [Melhauser and Zhang \(2014\)](#) emphasized nighttime destabilization of the local and large-scale environment through radiative cooling, while the proposed mechanism by [Nicholls \(2015\)](#) is a refinement of the second mechanism mentioned above through which circulations generated can have significant influences on convective activity in the TC core. Despite clear observational evidence of diurnal variations of TC cloud canopies (e.g., [Dunion et al. 2014](#)), how the diurnal radiation cycle impacts, and what the impacts are on, mature tropical cyclones including structure, intensity,<sup>1</sup> and associated rainbands remains mostly unexplored with complex numerical models. The

current study seeks to address the impact of the diurnal radiation throughout the life cycle of an observed TC ([Hurricane Edouard 2014](#)) from its formation to maturity using convection-permitting simulations that explore all of the three aforementioned mechanisms on the role of radiative forcing on deep convection.

This paper is organized as follows. The model setup and experimental design of the control and sensitivity experiments are described in [section 2](#). Overview of the evolution of Hurricane Edouard (2014) is provided in [section 3](#). Impacts of the diurnal radiation cycle on the formation and early development stage of Edouard are shown in [section 4](#), while the rapid intensification (RI) and mature stages are presented in [section 5](#). Concluding remarks follow in [section 6](#).

## 2. Model setup and experimental design

### a. WRF and the control simulation

The nonhydrostatic Advanced Research version of the Weather Research and Forecasting Model (ARW), version 3.5.1 ([Skamarock et al. 2008](#)), is used in this study. The horizontal grid spacing and coverage, from coarse to fine domains, is D01: 27 km,  $379 \times 244$ ; D02: 9 km,  $298 \times 298$ ; and D03: 3 km,  $298 \times 298$ . All three domains have 43 vertical terrain-following Eta levels with model top at 10 hPa. The inner domains (D02 and D03) are two-way nested and vortex following. The Rapid Radiation Transfer Model (RRTM) longwave radiative scheme ([Mlawer et al. 1997](#)), Dudhia shortwave (SW) radiation scheme ([Dudhia 1989](#)), the WRF single-moment 6-class microphysics scheme ([Hong and Lim 2006](#)), and Yonsei University (YSU) planetary boundary layer (PBL) scheme ([Hong et al. 2006](#)) are employed for all domains. The Grell–Freitas cumulus scheme ([Grell and Freitas 2014](#)) is used for D01; no cumulus parameterization is used for D02 and D03. The interaction between the radiation and microphysics scheme is the same as described in [Melhauser and Zhang \(2014\)](#).

The control simulation (CNTL) is initialized with composite-mean initial conditions from the 10 best-performing ensemble members in terms of intensity selected from a 60-member 126-h ensemble that is directly from The Pennsylvania State University (PSU) real-time WRF ensemble Kalman filter (WRF–EnKF) analysis and forecast system starting at 1200 UTC 11 September 2014 ([Zhang and Weng 2015](#); [Weng and Zhang 2016](#)). The PSU WRF–EnKF ensemble is part of NOAA’s Hurricane Forecast Improvement Project (HFIP) with detailed system configurations and forecasts (as well as archives of this event; available at

---

<sup>1</sup> Following [Holland and Merrill \(1984\)](#), in this study, TC “intensity” is defined by the maximum 10-m azimuthal wind speed or by the minimum central pressure. “Strength” is defined by the average relative angular momentum of the low-level circulation (inside 300-km radius). “Size” is defined by the axisymmetric extent of gale force winds. Here volume-averaged kinetic energy ( $\text{m}^2 \text{s}^{-2}$ ) within radius of 270 km and radius of azimuthally averaged wind speed of 34 or 50 kt at 10-m level can also be used to represent strength and size, respectively.

TABLE 1. Description of experiments set up in the study.

Name	Start time	Integration hours	Radiation	
			Solar shortwave	Longwave
CNTL	1200 UTC 11 Sep	168	Normal diurnal cycle	Normal
NoSolarRad0h	1200 UTC 11 Sep	126	Off	Normal
ConstSolarRad0h	1200 UTC 11 Sep	126	Fixed at local noon	Normal
NoSolarRad48h	1200 UTC 13 Sep	78	Off	Normal
ConstSolarRad48h	1200 UTC 13 Sep	78	Fixed at local noon	Normal
NoSolarRad72h	1200 UTC 14 Sep	96	Off	Normal
ConstSolarRad72h	1200 UTC 14 Sep	96	Fixed at local noon	Normal
NoSolarRad96h	1200 UTC 15 Sep	72	Off	Normal
ConstSolarRad96h	1200 UTC 15 Sep	72	Fixed at local noon	Normal

the website [hfip.psu.edu](http://hfip.psu.edu)). The PSU real-time system is also used to provide high-resolution forecast guidance to NASA's field campaign of Hurricane and Severe Storm Sentinel (HS3) during which Hurricane Edouard developed.

The WRF–EnKF system is initialized at 1200 UTC 07 September 2014 with the operational Global Forecast System (GFS) analysis, and the first data assimilation is conducted over all three domains at 0000 UTC 8 September after 12 h of ensemble integration. The system performs cycling assimilation every 3 h until Edouard dissipates (1800 UTC 19 September). The operational GFS forecasts from 6 h prior are used as lateral boundary conditions for the deterministic forecast, while the ensemble lateral boundary conditions are generated by adding perturbations derived from the background error covariance of the WRF variational (WRF-VAR) data assimilation system (Barker et al. 2004) to the deterministic lateral boundary conditions. The control simulation is initialized with the composite initial conditions from the 10 best-performing members from 1200 UTC 11 September that is integrated for 168 h using the GFS forecast as the boundary conditions at the outermost grid.

### b. Sensitivity experiments

Four sets of sensitivity experiments (Table 1) are conducted to elucidate the effects of the diurnal radiation cycle on different stages of the hurricane life cycle, from the initial development to rapid intensification and maturity at peak intensity. An endless daytime simulation with the solar insolation set at local noon (“ConstSolarRad”) and an endless nighttime simulation with no solar insolation (“NoSolarRad”) are included in each set of these sensitivity experiments, starting at 0, 48, 72, 96 model integration hours of the control simulation, which grossly represent the beginning time of genesis, early development, rapid intensification, and mature stages of Edouard, respectively. These sensitivity experiments are designed to isolate the two extremes of diurnal radiation forcing but without the diurnal cycle.

### c. Storm tracking

The Geophysical Fluid Dynamics Laboratory (GFDL) vortex tracker (Marchok 2002; Tallapragada et al. 2013) is used to track the center of Edouard. The storm center is tracked by searching for the average of the maximum or minimum of several parameters near an input first-guess position of the targeted vortex. The primary fields used for tracking are relative vorticity and geopotential height at 850 and 700 hPa and the minimum sea level pressure. The horizontal wind speed at 10 m, 850 hPa, and 700 hPa are also used in the tracking but in a supplementary role. Winds at 500 hPa are used, along with other parameters, for advecting the storm and creating a first-guess position next time. Best-track data (Stewart 2014) are used at the initial time of 1200 UTC 11 September as the first-guess position of the storm center. Diagnostic analyses are all performed on the 3-km domain (D03) unless otherwise noted.

## 3. Overview of evolution of Hurricane Edouard (2014)

The best track of Edouard's path is shown in Fig. 1a with the wind and pressure histories shown in Figs. 1b and 1d, respectively. By 1200 UTC 11 September, the system was designated as a tropical depression over the far eastern tropical Atlantic (Stewart 2014). The depression moved to the northwest and maintained that general motion for the next 5 days. The cyclone became a tropical storm early on 12 September and a hurricane early on 14 September. Edouard continued to intensify to a major hurricane early on 16 September, reaching its peak intensity of  $54 \text{ m s}^{-1}$  at 1200 UTC that day, which was followed by a weakening trend almost immediately. The control run nicely catches the general features of track and development in all stages of the lifetime mentioned above (Figs. 1a–d). Although Edouard's tracks covered two time zones during the simulations period, the local standard time (LST; UTC – 4 h) hereafter is

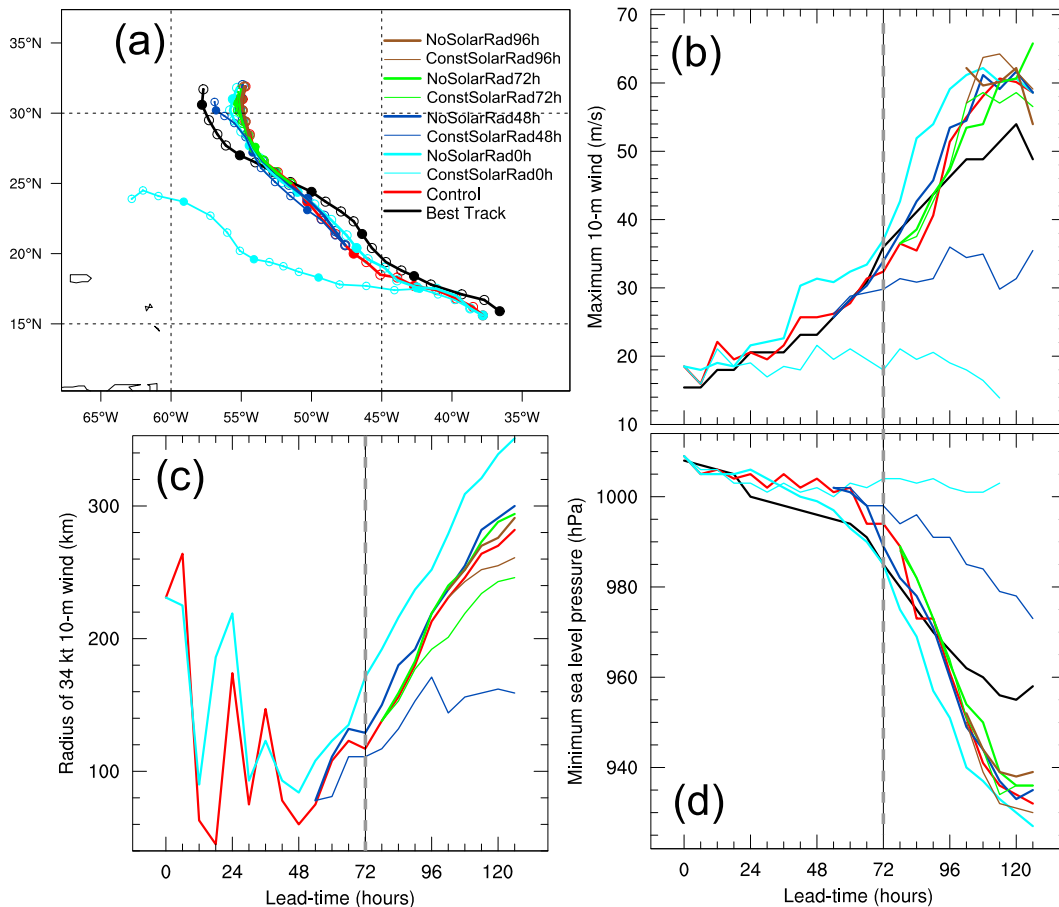


FIG. 1. (a) Tracks, (b) maximum 10-m wind speed ( $\text{m s}^{-1}$ ), (c) radius of azimuthally averaged 34-kt wind speed at 10-m level, and (d) minimum sea level pressure (hPa) evolutions of control simulation (red line) and sets of sensitivity experiments [see text for detail; bold (light) lines for NoSolarRad (ConstSolarRad) experiments], with comparison of NHC best-track data (black line). The period is from 1200 UTC 11 Sep to 1800 UTC 16 Sep. The circles on the tracks denote the location every 6 h. The gray dashed line denotes the time of rapid intensification in the control run roughly. The last 12-h data of ConstSolarRad0h is lacking because the storm circulation is too weak to be identified distinctly. The storm maximum wind of ConstSolarRad0h was too weak to approximate 34 kt only, so there is little significance to show in (c).

all based on the longitude of 60°W (Fig. 1a) for the simplicity of intercomparison.

The control simulation of Edouard shows obvious diurnal variation of outgoing longwave radiation (OLR) within 500 km of the vortex center from formation to mature stages (Fig. 2a). The lower OLR reflects deeper cloud, associated with more active convective activities, which parallels the infrared (IR) brightness temperature observed by satellites, since longwave radiation is partly absorbed by cloud and air from below. The diurnal pulses (lower OLR in Fig. 2a) formed in the storm inner core after sunset each day, then propagated away and reached a radius of several hundred kilometers from the cyclone center by the following afternoon.

Figure 3 shows an example of the TC diurnal cycle for Edouard from 1800 UTC (1400 LST) 15 September to

1800 UTC (1400 LST) 16 September. The 6-h IR brightness temperature trend shows that a pulse at radius of 300 km occurs in the early morning, then propagates outwards and reaches 400 km at around noon. A higher-frequency oscillation is present at the radius of  $\sim 200$  km. The control simulation closely reproduces the observed diurnal cycle of Edouard (made available to us through Chris Velden) and is consistent with past observational studies [Fig. 2 of Kossin (2002); Figs. 3, 6, 8, and 9 of Dunion et al. (2014)]. In contrast with the control run, there is no diurnal cycle feature of OLR in NoSolarRad0h (Fig. 2b) or ConstSolarRad0h (Fig. 2c) experiments during all the simulations due to shutting off the solar radiation or setting it as a constant. The effect of the diurnal cycle on the storm's early development is analyzed by sensitivity experiments with

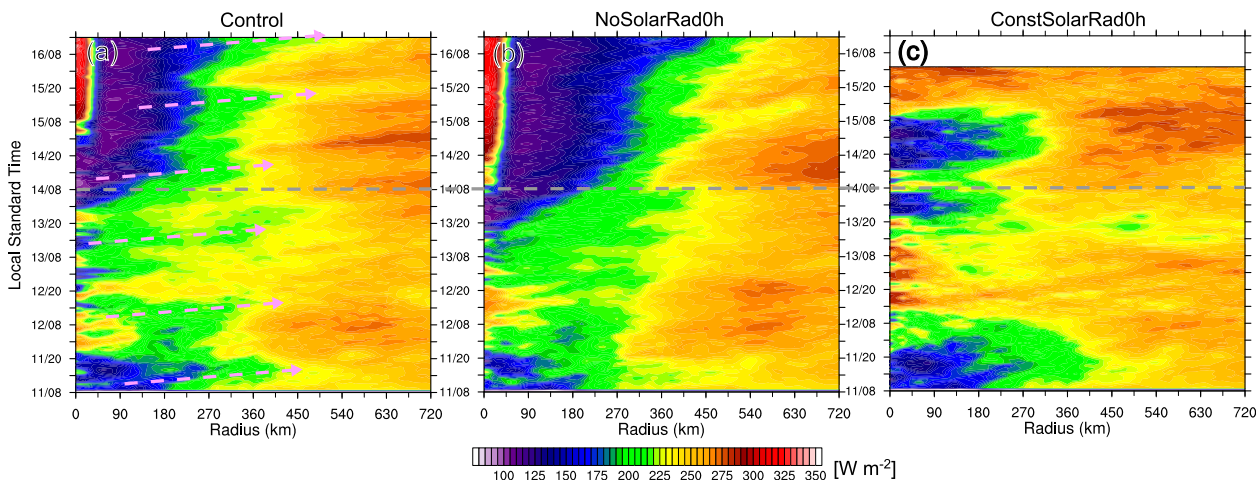


FIG. 2. (a) Hovmöller (radius vs LST) diagram of simulated azimuthally averaged OLR ( $\text{W m}^{-2}$ ) at top of atmosphere on domain 2 of control run. Purple arrows denote the diurnal pulses (see text for detail). (b) As in (a), but for NoSolarRad0h. (c) As in (a), but for ConstSolarRad0h. The period is from 1200 UTC (0800 LST) 11 Sep to 1800 UTC (1400 LST) 16 Sep. The gray dashed line denotes the time of rapid intensification in the control run roughly.

modified radiation starting at different times in an attempt to isolate the extremes of the diurnal radiation cycle, as described in section 2b. The impact on the intensities, sizes, and even tracks of these storms can be seen in Figs. 1a–d, spanning 11–16 September. It is easy to find out that responses to the diurnal cycle of solar radiation forcing have differences in extent and feature throughout the different stages of tropical cyclones through comparisons between sets of sensitivity experiments. The following two sections will describe these impacts in different stages of Edouard in detail.

**4. Impact on intensification rate in formation stages**

In this section the diurnal radiation cycle impact in the formation stages of Edouard will be investigated through comparing the CNTL simulation with the sensitivity experiments NoSolarRad0h and ConstSolarRad0h. CNTL and NoSolarRad0h both developed the hurricane, with CNTL having track and intensity to the best-track estimate while the NoSolarRad0h simulation intensified more rapidly and was more intense than the CNTL run after 36 h (Figs. 1b,d). In contrast, ConstSolarRad0h failed to form a TC during the 126-h integration; the tropical disturbance was substantially weaker than CNTL after 36 h and cannot be easily tracked after 114 h (Figs. 1a–d). Without developing to an organized storm, the low pressure disturbance took a much more leftward track than the observed storm, gradually drifting more westward after 24 h in ConstSolarRad0h instead of a more northwestward track in CNTL (best-track observations); this is likely due to the influence of the effective steering layer, tied to the storm

intensity, which is shallower for the weaker TC according to Velden and Leslie (1991). The track may also be due to a stronger beta effect associated with a stronger TC in CNTL (Holland 1983; Fang and Zhang 2012; Qian et al. 2013).

We first examine the influence of diurnal radiation cycle during the formation and subsequent development stages by diagnosing the difference in the local environment (within 180 km of the storm center) between CNTL and the two sensitivity experiments starting at 0 h.

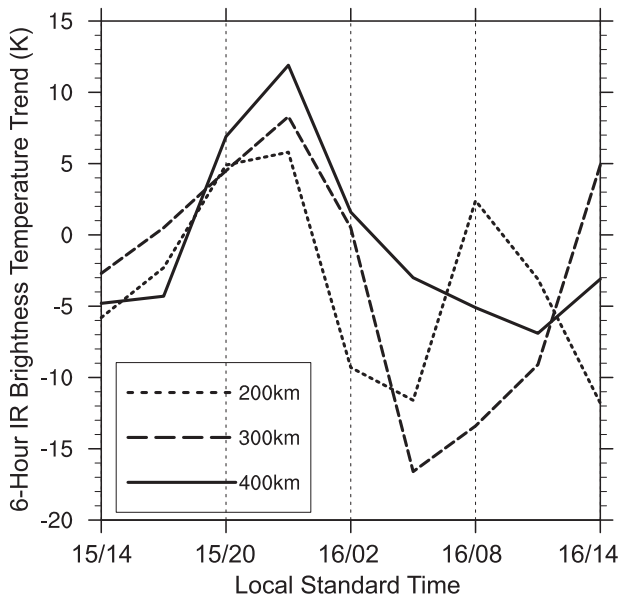


FIG. 3. Azimuthally averaged IR 6-h brightness temperature trends at 200-, 300-, and 400-km radii around the storm for the control run from 1800 UTC (1400 LST) 15 Sep to 1800 UTC (1400 LST) 16 Sep.

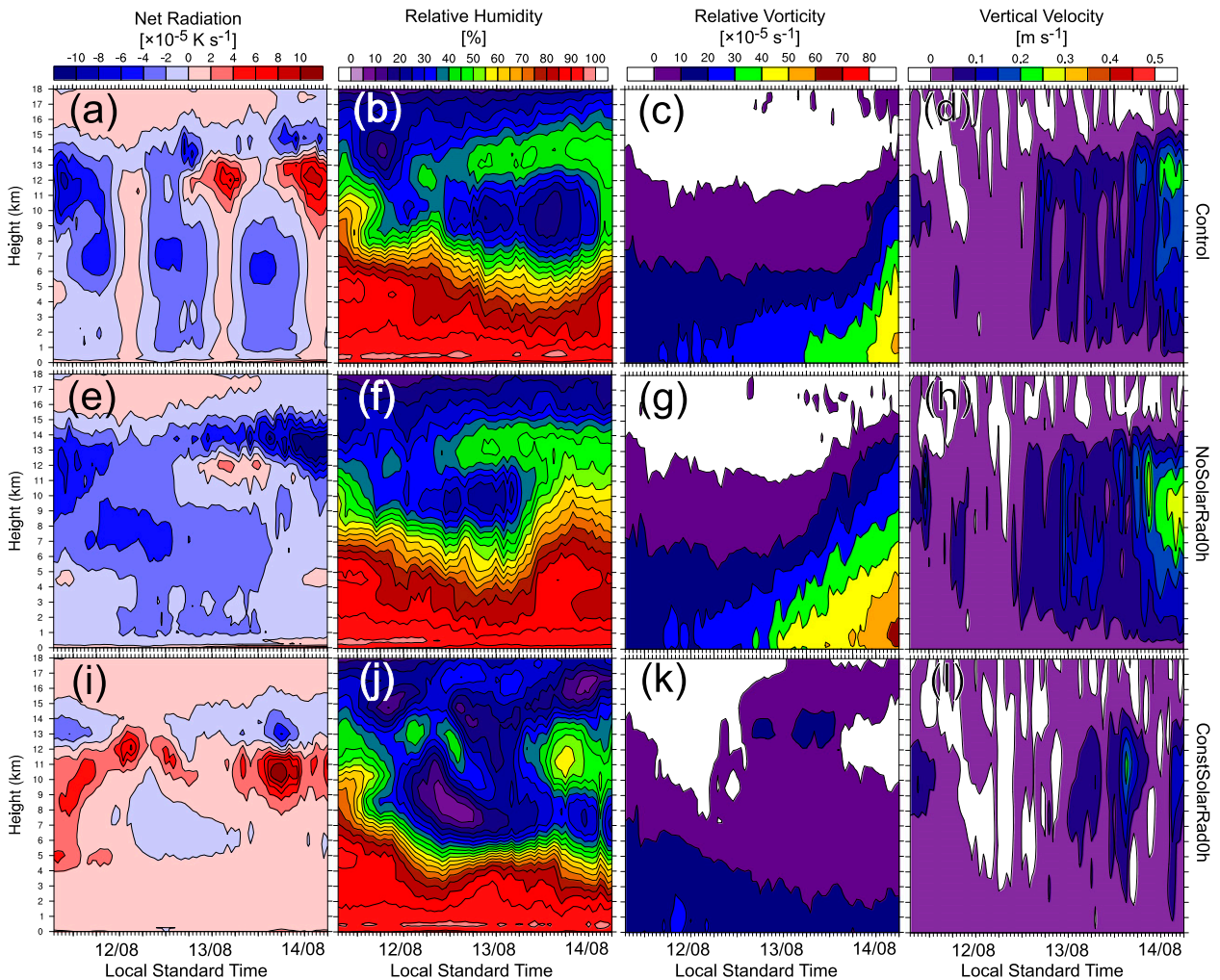


FIG. 4. Vertical profiles of the average local-environment hourly model output within 180 km of the vortex center of (a),(e),(i) net radiation, (b),(f),(j) relative humidity, (c),(g),(k) relative vorticity, and (d),(h),(l) vertical velocity for (top) control run and sensitivity experiments (middle) NoSolarRad0h and (bottom) ConstSolarRad0h. The period is from 1900 UTC (1500 LST) 11 Sep to 1800 UTC (1400 LST) 14 Sep.

Figure 4 shows the vertical profiles of the average local-environment hourly model output of net radiation forcing (i.e., potential temperature tendency due to the sum of longwave and shortwave radiation), relative humidity, relative vorticity, and vertical velocity from 1900 UTC (1500 LST) 11 September to 1800 UTC (1400 LST) 14 September for experiments CNTL, NoSolarRad0h, and ConstSolarRad0h. In the CNTL run, the net radiation forcing has an evident diurnal cycle in the troposphere, with maximum potential temperature tendency occurring at 1200–1300 LST each day, shortly after the strongest solar insolation (Fig. 4a). Before 1200 UTC (0800 LST) 12 September, the profiles have negative net radiation forcing throughout the troposphere. This is similar to the average profiles of the clear-sky region in Figs. 9a and 9d of Melhauser and Zhang

(2014), and it is attributable to the dearth of cloud, water, and ice in the core area during the formation stage. As the system developed into a tropical storm, the profiles of net radiation forcing gradually shifted toward a more cloudy type of vertical profile displayed in Figs. 9a and 9d of Melhauser and Zhang (2014): there are mostly negative values at the top of the cirrus canopy and mostly positive values below in CNTL (Fig. 4a). In NoSolarRad0h (Fig. 4e) and ConstSolarRad0h (Fig. 4i), there are no apparent signals of diurnal variations in net radiation. Nevertheless, the net radiative forcing is much more negative in NoSolarRad0h than that in ConstSolarRad0h; shutting off solar insolation in NoSolarRad0h leads to an effective net radiative cooling in NoSolarRad0h in comparison to ConstSolarRad0h (and to somewhat a lesser degree to CNTL).

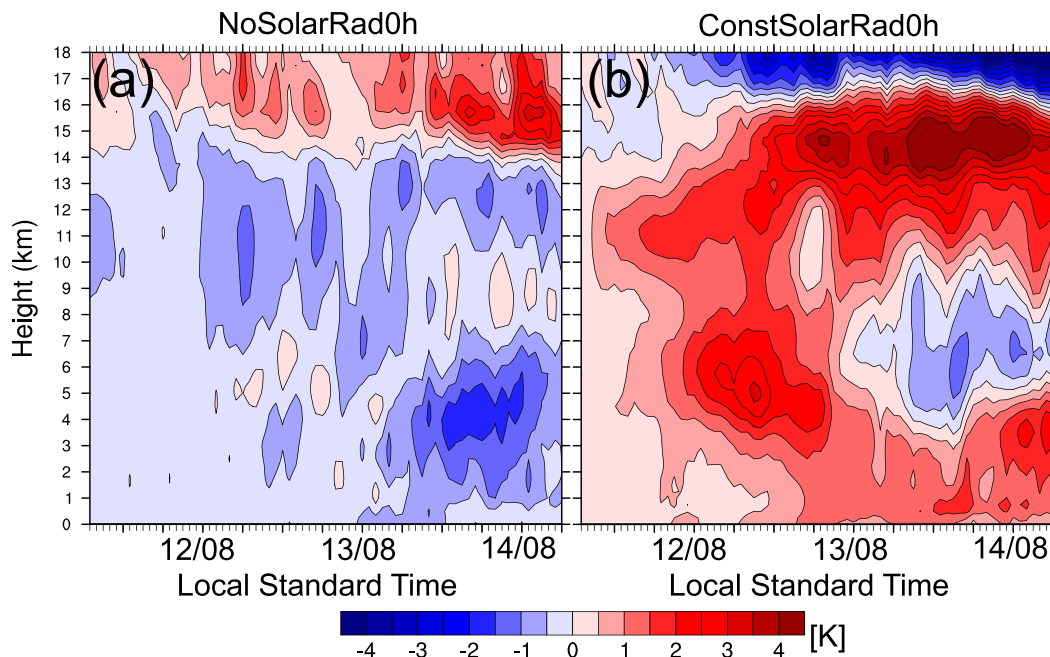


FIG. 5. Time evolution of the vertical profile of temperature difference (K) averaged within 180 km of the vortex center for (a) NoSolarRad0h minus CNTL and (b) ConstSolarRad0h minus CNTL. The period is as in Fig. 4.

With persistent maximum solar insolation, ConstSolarRad0h (Fig. 4j) has a decrease in relative humidity from 4 to 9 km when compared to CNTL (Fig. 4b) and more so to NoSolarRad0h (Fig. 4f). The constant heating of maximum shortwave radiation resulted in a net mid- to upper-tropospheric warming in ConstSolarRad0h and increased the temperature (Fig. 5b), which is primarily responsible for a smaller relative humidity compared to CNTL (Fig. 4b) and NoSolarRad0h (Fig. 4f); this is pronounced before and during the genesis of Edouard from 0600 UTC (0200 LST) 12 September to 0600 UTC (0200 LST) 13 September. Midlevel warming and drying of the local environment for ConstSolarRad0h suppressed the potential for strong convective bursts that occurred in CNTL and NoSolarRad0h and were essential to the formation of the storm. Conversely, NoSolarRad0h was the earliest to moisten the levels from 5 km up to the outflow layer because of net radiative cooling and subsequent moisture transport for more vigorous deep convection, beginning at 1800 UTC (1400 LST) 13 September (Fig. 4f). Once the midlevel (about 7–8 km) diabatic heating from convection exceeded the net radiative cooling, the temperature became higher in CNTL (and NoSolarRad0h) than in ConstSolarRad0h after 1200 UTC (0800 LST) 13 September as shown in Figs. 5a and 5b.

The relative vorticity (Figs. 4c,g,k) and vertical velocity (Figs. 4d,h,l) are similar for CNTL, ConstSolarRad0h, and NoSolarRad0h during the first 18 h. Thereafter, the

relative vorticity in both CNTL and NoSolarRad0h increased steadily from the low level upward but there was no discernible increase in ConstSolarRad0h. The enhancement of the low-level vorticity in both experiments with a net nocturnal radiative cooling phase can likely be ascribed to the enhanced stretching that enhances the convergence of ambient vorticity owing to enhanced moist convection, as was noted in the genesis of Hurricane Dolly (2008) and other tropical cyclones (e.g., Fang and Zhang 2010). On the contrary, convective activity is evidently suppressed by midlevel drying and warming in ConstSolarRad0h, resulting in a disorganized vortex that failed to develop into a TC during the 126-h integration.

The storm's evolution and structure are also notably different amongst the three experiments, as can be seen from the azimuthal mean structure averaged over three consecutive 24-h periods (Fig. 6). The secondary circulation is much stronger in NoSolarRad0h (Figs. 6d–f) than that in CNTL (Figs. 6a–c), with stronger boundary layer inflow, upper-layer outflow, and vertical upward motions, all of which are much weaker in ConstSolarRad0h than CNTL during the first three days of the simulation (Figs. 6g–i). The maximum radial inflow gradually increases while moving inwards closer to the vortex core region in both NoSolarRad0h and CNTL, but it is always outside of about 200 km from the center in ConstSolarRad0h. In the meantime, the radius of maximum tangential wind (RMW) at the surface contracts from about 230 to 50 km in both NoSolarRad0h

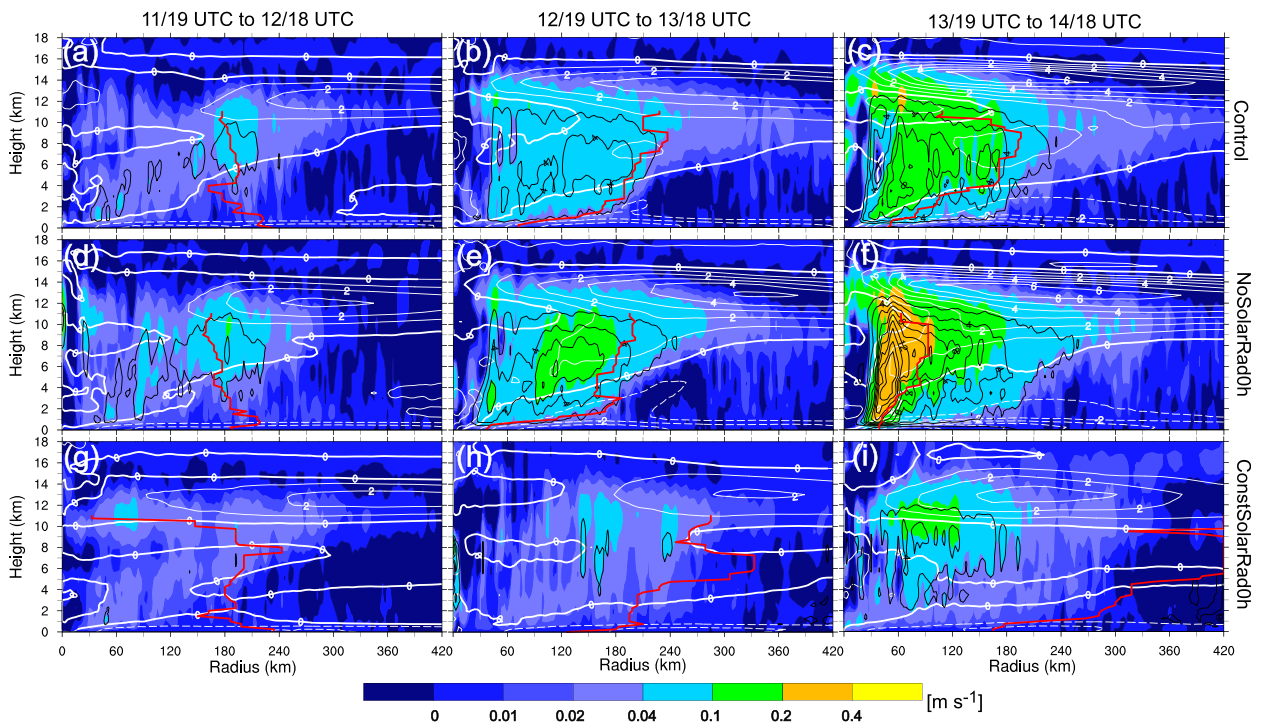


FIG. 6. The 24-h-average azimuth-mean vertical cross sections of vertical velocity (shading), radial velocity (white contours at interval of  $1 \text{ m s}^{-2}$ ; solid, dashed, and bold denote positive, negative, and zero, respectively), and latent heating (black contours at interval of  $2 \times 10^{-4} \text{ K s}^{-1}$ ) for experiments of (a)–(c) CNTL, (d)–(f) NoSolarRad0h, and (g)–(i) ConstSolarRad0h from (left) 1900 UTC 11 Sep to 1800 UTC 12 Sep, (center) 1900 UTC 12 Sep to 1800 UTC 13 Sep, and (right) 1900 UTC 13 Sep to 1800 UTC 14 Sep. Superposed red lines denote RMW at levels of 0–11 km for each panel.

(Figs. 6d–f) and CNTL (Figs. 6a–c). No RMW contraction but a gradual increase of the RMW during the 72-h simulation further indicates a nondeveloper in ConstSolarRad0h (Figs. 6g–i).

In brief summary, the above analyses show that the net nighttime radiative cooling results in midlevel moistening and destabilization in the incipient vortex core area and surrounding larger-scale environment during the early development period that promotes deeper and stronger moist convection and subsequent stronger convergence of ambient vorticity (through enhanced stretching), which eventually leads to the formation of Edouard in both CNTL and NoSolarRad0h. It should also be noted that the impact of diurnal radiative forcing on the thermodynamic and dynamic field is an integrated effect since the three simulations diverge little during the first 12–18 h (Figs. 1 and 4). It takes considerable time for the difference in radiative forcing in the sensitivity experiments to substantially alter the thermodynamic and dynamic fields associated with the incipient storm; thus, the switch-on or -off of solar insolation between day and night in CNTL is a rather gradual and even lagged response rather than a sharp transition.

The effect of net nighttime radiative cooling in promoting enhanced deep moist convection continues to play an important role in the storm’s development and intensification even after Edouard in the CNTL simulation reaches tropical storm strength, as shown by comparison with the sensitivity experiments of the NoSolarRad48h and ConstSolarRad48h in Fig. 7. These two new sensitivity experiments are performed exactly the same as NoSolarRad0h and ConstSolarRad0h except that the solar isolation is switched off, respectively, or permanently in maximum phase starting from 1200 UTC (0800 LST) 13 September, which is 48 h into the CNTL simulation, when the maximum 10-m wind speed of the storm had already reached above  $25 \text{ m s}^{-1}$  (Fig. 1b).

Although the diurnal radiation cycle at this stage did not lead to a significant difference in Edouard’s track between both sensitivity experiments and CNTL (Fig. 1a), it continues to have an important impact on the strengthening and size increasing of the storm (Figs. 1b–d); the maximum 10-m wind speed of ConstSolarRad48h barely reached the threshold of a hurricane (though with some strengthening even after switching on permanent maximum solar insolation) while NoSolarRad48h develops

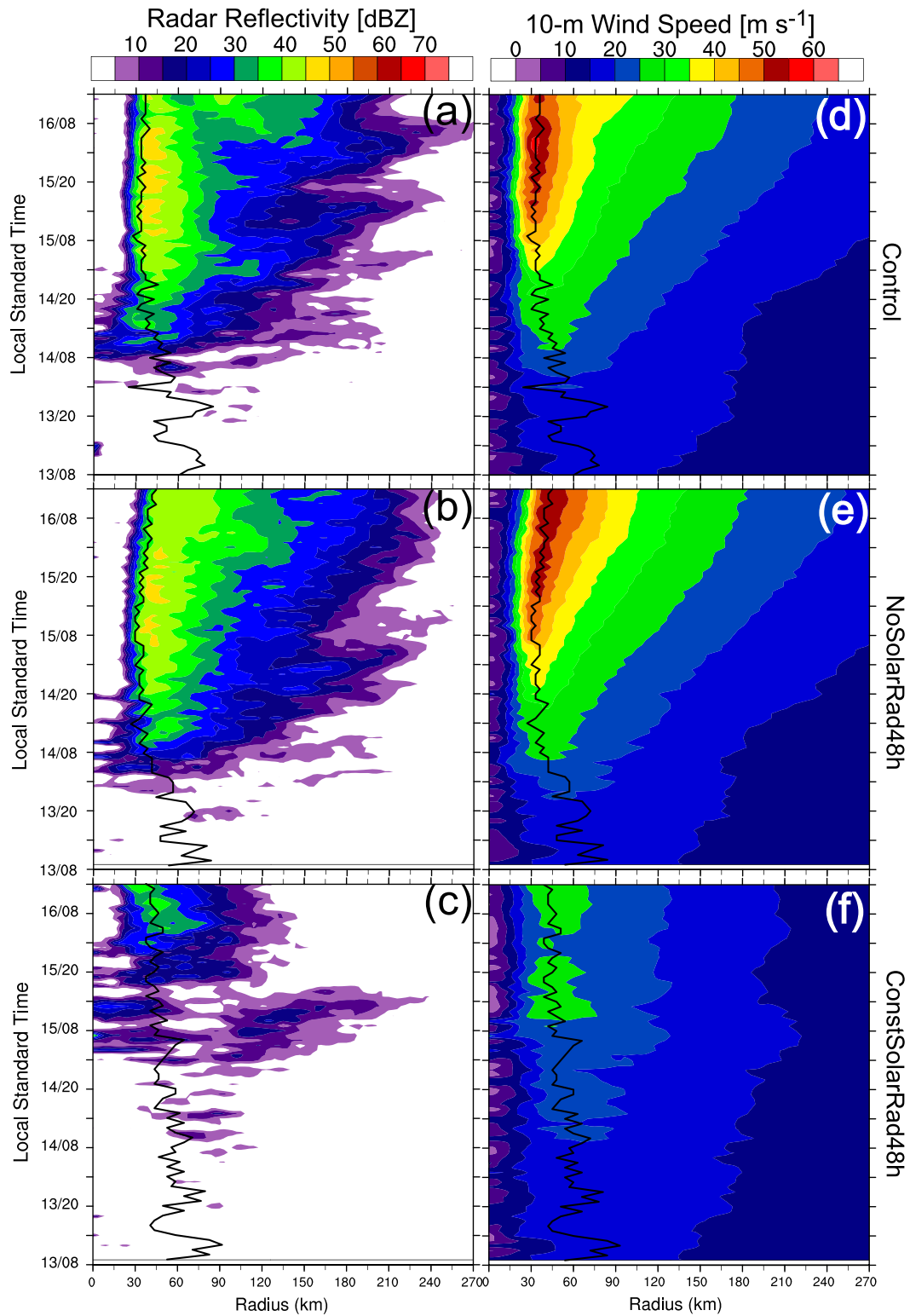


FIG. 7. Time evolution of azimuthally averaged (a)–(c) column-maximum radar reflectivity (dBZ) and (d)–(f) 10-m wind speed ( $\text{m s}^{-1}$ ) for (top) CNTL, (middle) NoSolarRad48h, and (bottom) ConstSolarRad48h. The solid black lines denote the radii of maximum 10-m wind. The period is from 1200 UTC (0800 LST) 13 Sep to 1800 UTC (1400 LST) 16 Sep.

into a major hurricane as in CNTL (and best-track observations) (Figs. 1b,d). As indicated by the azimuthally averaged simulated radar reflectivity in Figs. 7a–c, convective activities in both the inner-core area and the outer rainbands are much weaker in ConstSolarRad48h than CNTL (and even more so than NoSolarRad48h). Consequently, without a night phase of net radiative cooling, ConstSolarRad48h only has slow and moderate strengthening while both CNTL and NoSolarRad48h soon begin eyewall (RMW) contraction and RI as observed (Figs. 1b,d and 7d–f). NoSolarRad48h (ConstSolarRad48h) also has a bigger (smaller) size than CNTL as a result of more (less) active convection in a moister (drier) environment (Fig. 1c). The reason for the size difference between sensitivity experiments of solar radiation will be analyzed in detail in the next section.

### 5. Impact of the diurnal cycle on storm structure and strength after the start of RI

In this section, the effect of diurnal radiative forcing on the RI and mature stages of Edouard will be analyzed through comparison of sensitivity experiments NoSolarRad72h and ConstSolarRad72h with the CNTL simulation. NoSolarRad72h (ConstSolarRad72h) is performed by switching off (staying permanently on the maximum phase of) the solar insolation from 1200 UTC (0800 LST) 14 September, which is 72 h into the CNTL simulation when the maximum 10-m wind speed of the storm had already reached hurricane intensity (Figs. 1b,d). The storm begins its RI around 1200 UTC (0800 LST) 14 September in the CNTL simulation, approximately the start of the sensitivity experiments that either have no solar insolation (NoSolarRad72h) or permanent peak solar insolation (ConstSolarRad72h).

#### a. Evolution of hurricane structure and strength after the start of RI

Unlike the sensitivity experiments that switch-off or permanently on solar insolation during the formation and earlier development stages, both NoSolarRad72h and ConstSolarRad72h simulated the track and intensity of Edouard (in terms of maximum 10-m surface wind speed) very similar to those of the CNTL simulation (Fig. 1). Also similar are the contractions of eyewall and RMW as well as the timing and rate of RI among all three experiments (Figs. 1b,d, 8a–c, and 9a): the RMW shrunk from around 45 to 30 km at around 0000 UTC 15 (2000 LST 14) September (Fig. 9a) when a clear eye formed in each simulation (Figs. 8a–c), about 12 h after the start of RI.

Nevertheless, there are also clear differences among these simulations with and without the diurnal radiation

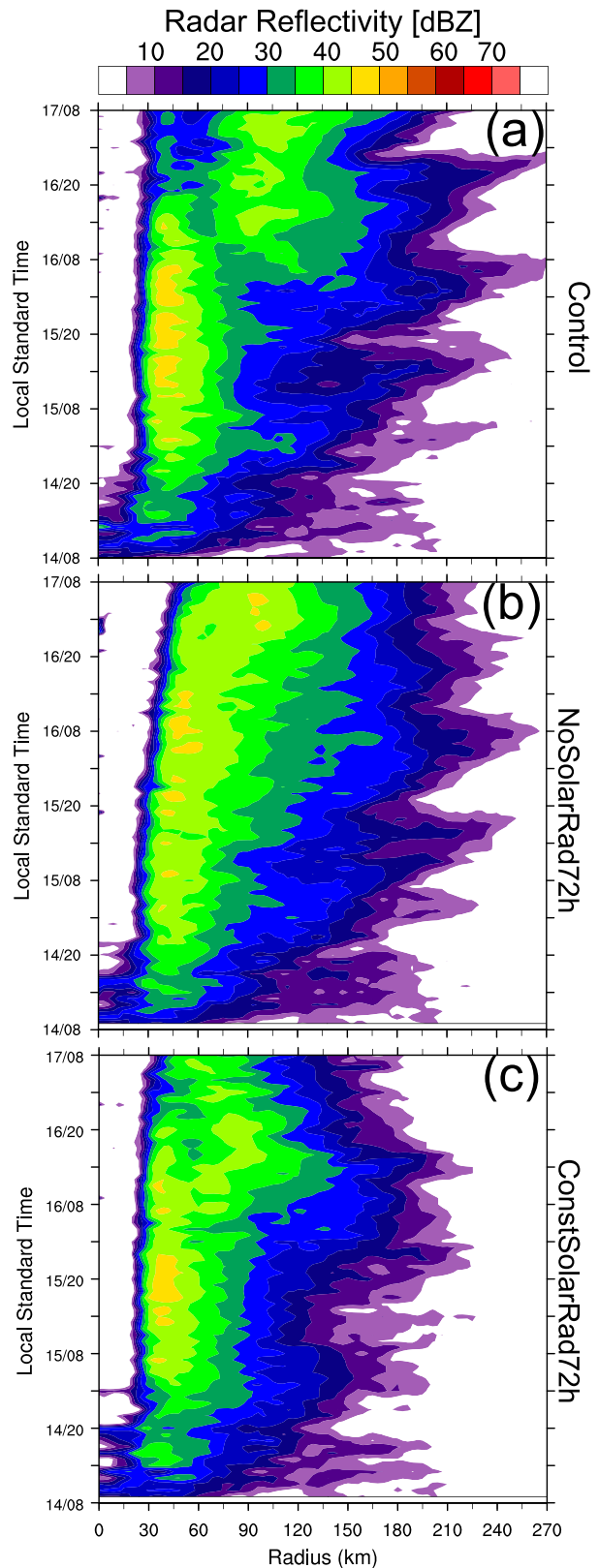


FIG. 8. Time evolution of azimuthally averaged column-maximum radar reflectivity (dBZ) for (a) CNTL, (b) NoSolarRad72h, and (c) ConstSolarRad72h. The period is from 1200 UTC (0800 LST) 14 Sep to 1200 UTC (0800 LST) 17 Sep.

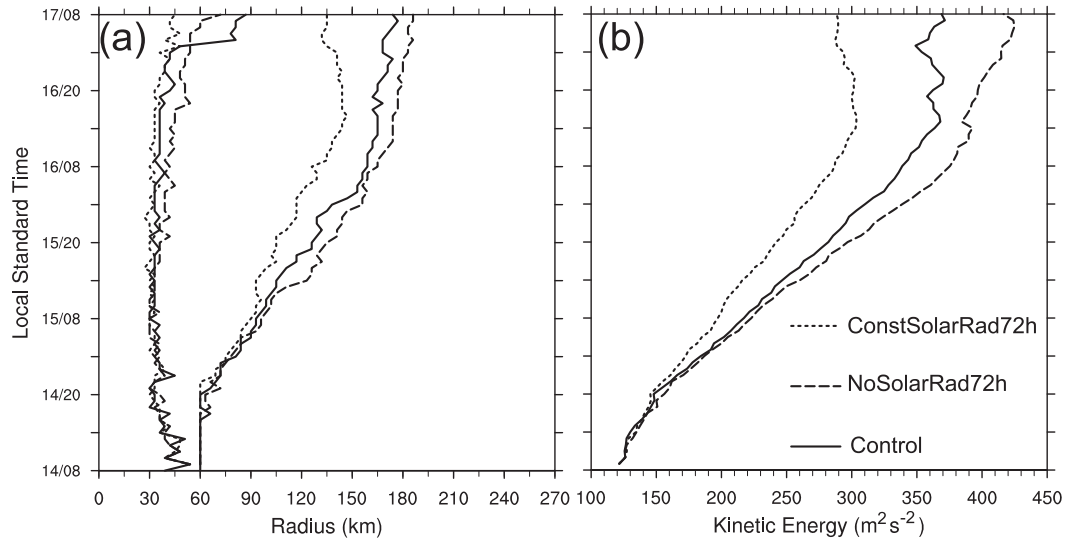


FIG. 9. (a) Time evolution of radii of maximum (left lines) and  $26 \text{ m s}^{-1}$  (i.e., 50 kt; right lines) azimuthally averaged 10-m wind speed and (b) time evolution of volume-averaged kinetic energy ( $\text{m}^2 \text{s}^{-2}$ ) at 10-m level within radius of 270 km in CNTL, NoSolarRad72h, and ConstSolarRad72h experiments. The period is from 1200 UTC (0800 LST) 14 Sep to 1200 UTC (0800 LST) 17 Sep.

cycle as well as with and without solar insolation. In particular, convective activities are the strongest in NoSolarRad72h (owing to net radiative cooling), especially those outside of the primary eyewall, while ConstSolarRad72h has the weakest and least expansive outer rainbands, soon after the start of the sensitivity experiments and more evident 18 h after the start of the RI in all simulations (Figs. 8a–c). More rigorous convective activities after RI subsequently led to the gradual expansion of eyewall and primary rainbands in NoSolarRad72h (Figs. 8b and 9a), resulting in a much bigger hurricane in terms of both RMW and the outside radius of 50-kt ( $1 \text{ kt} = 0.51 \text{ m s}^{-1}$ ) wind at around 1800 UTC 16 September in NoSolarRad72h (Fig. 10b) than in ConstSolarRad72h (Fig. 10c), the latter of which has no noticeable change in the eye size and RMW during this period (Figs. 8c, 9a, and 10c). The volume-averaged kinetic energy (KE) [cf. the definition of total KE in Eq. (2) of Maclay et al. (2008)] at the 10-m level within the radius of 270 km in Fig. 9b further shows that enhanced convection with the persistent night phase of radiative cooling also results in a hurricane with greater strength (cf. NoSolarRad72h than ConstSolarRad72h).

Moreover, interestingly, the azimuthally averaged column-maximum reflectivity field shows evidence of a secondary eyewall formation (SEF) contracting from about 120 km inwards to 90 km beginning at around 1200 UTC (0800 LST) 16 September in CNTL (Fig. 8a), but not in NoSolarRad72h (Fig. 8b). There are also some hints of the SEF in the sharp increasing of the RMW in CNTL [at 0600 UTC (0200 LST) 17 September of the

simulation, Fig. 9a] as well as in the snapshot of the horizontal distribution of the reflectivity field (Fig. 10a). The observed Edouard in real world also underwent SEF at similar times (Stewart 2014). The SEF can also be found in ConstSolarRad72h (Fig. 8c), although the outer eyewall is narrower and contracts inward more evidently, while the moat is less evident than in CNTL. After the replacement of the primary eyewall, the eye is smaller in ConstSolarRad72h than in CNTL (Figs. 10d,f), since the new eyewall contracts much farther inward in ConstSolarRad72h than CNTL (Figs. 8a,c). The average eye radius is largest for NoSolarRad72h, which experiences continuous expansion of the primary eyewall (without eyewall replacement) throughout the model integration (Figs. 8b and 10e). However, it is beyond the scope of the current study to examine the dynamics of the SEF and subsequent eyewall replacement cycle of Edouard for both the observed storm and in the CNTL. Nevertheless, the start of the SEF in CNTL and the lack of it in NoSolarRad72h suggest a potential role of diurnally varying radiation cycle, especially the solar insolation, in the TC's eyewall replacement cycle that certainly warrants future studies.

#### b. Radiation's role on convection in Edouard

The above analyses suggest that enhanced outer-core convective activities (and their diabatic heating release) associated with cloud–radiative forcing can broaden the cyclonic flow in the lower troposphere as well as augment the secondary circulation, which is to a certain extent consistent with previous findings such as in Wang

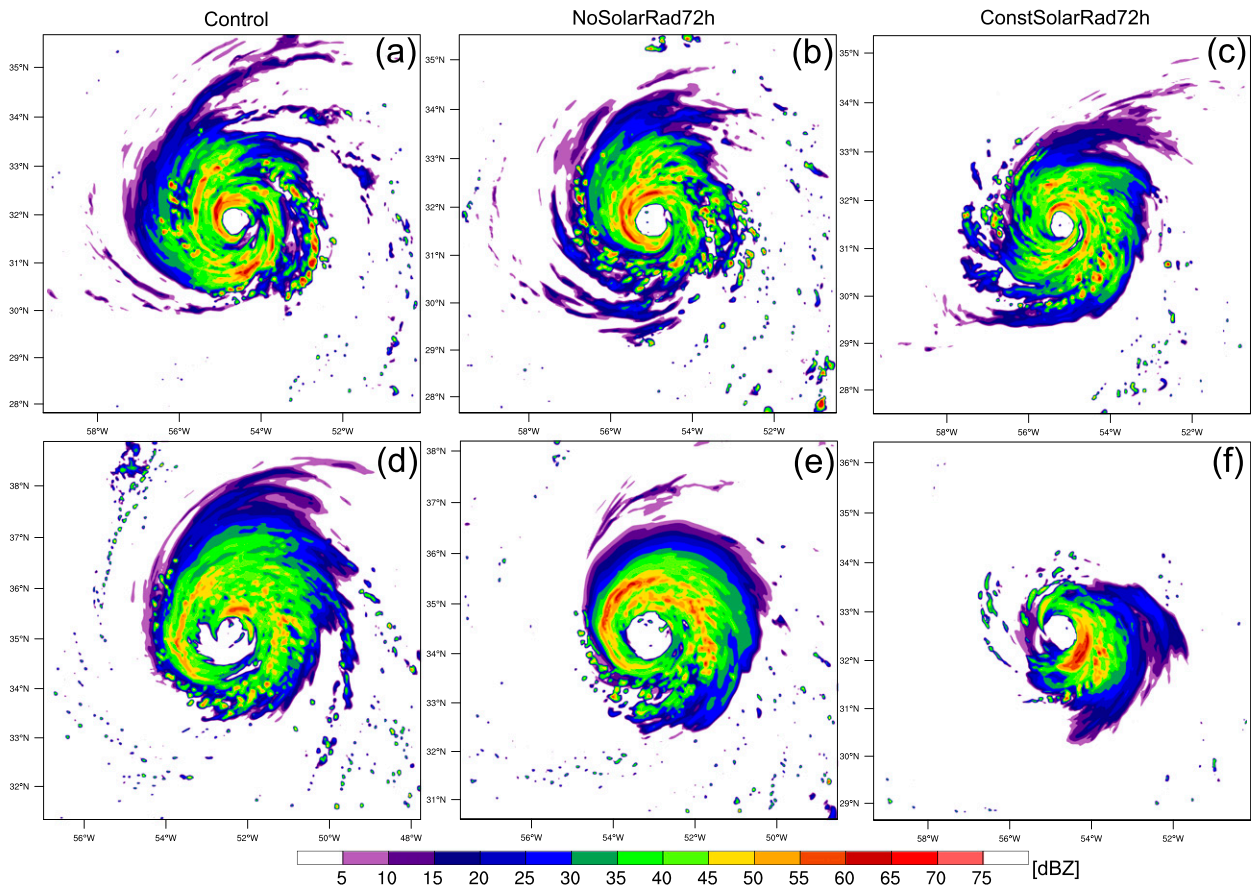


FIG. 10. Snapshots of column-maximum radar reflectivity of domain 3 on (a)–(c) 1800 UTC 16 Sep and (d)–(f) 1200 UTC 17 Sep for simulations of (left) CNTL, (center) NoSolarRad72h, and (right) ConstSolarRad72h.

(2009), Xu and Wang (2010), Fang and Zhang (2012), and Bu et al. (2014). More detailed analysis of the impact of diurnal radiation forcing and its impacts before the secondary eyewall formation are provided through a comparison with the three experiments.

The net radiative forcing in CNTL shows evident diurnal variation in both the eyewall and the outer-core region with maxima near the local noon time each day due to the solar shortwave heating (Figs. 11a,b). The maximum net radiative cooling is located at the level of 14–16 km within the radii of 30–60 km (Fig. 11a) and at 13–14-km height from outside the eyewall to the 180-km radius (Fig. 11b); the maximum net radiative warming is at the level of 10–13 km. These results are consistent with the vertical profiles of cloudy-air net radiative forcing in previous studies (e.g., Dudhia 1989; Melhauser and Zhang 2014; Bu et al. 2014). The increasing eyewall radiative cooling at the layer of 7–13 km during the night of 16 September (Fig. 11a) corresponds to the maximum intensity in terms of the maximum 10-m wind speeds (Fig. 1b). In the

ConstSolarRad72h experiment, the net radiative warming prevails below 13 km with the maximum at about 11–12 km (Figs. 11e,f) as a result of uninterrupted solar shortwave radiation. The radiative heating leads to the temperature increasing at higher levels, which is in strong contrast to CNTL and NoSolarRad72h (Figs. 12c,d). There is hardly any net radiative heating in the troposphere in NoSolarRad72h, resulting in net radiative cooling in the inner core and surrounding areas all the time (Figs. 11c,d). It can also be seen that the lowering of the cloud tops (Figs. 13c and 15f) is accompanied by a decrease in the height of maximum radiative cooling (Fig. 11c) when the eyewall begins to expand outward from 1900 UTC (1500 LST) 15 September to 1800 UTC (1400 LST) 16 September (Fig. 8b).

The temperature difference of ConstSolarRad72h and NoSolarRad72 minus CNTL will further indicate the effect of solar shortwave radiation on the thermodynamic stratification (Fig. 12). In the outer core of 60–180 km, the temperature is higher below the level of about 15 km in ConstSolarRad72h than CNTL with the

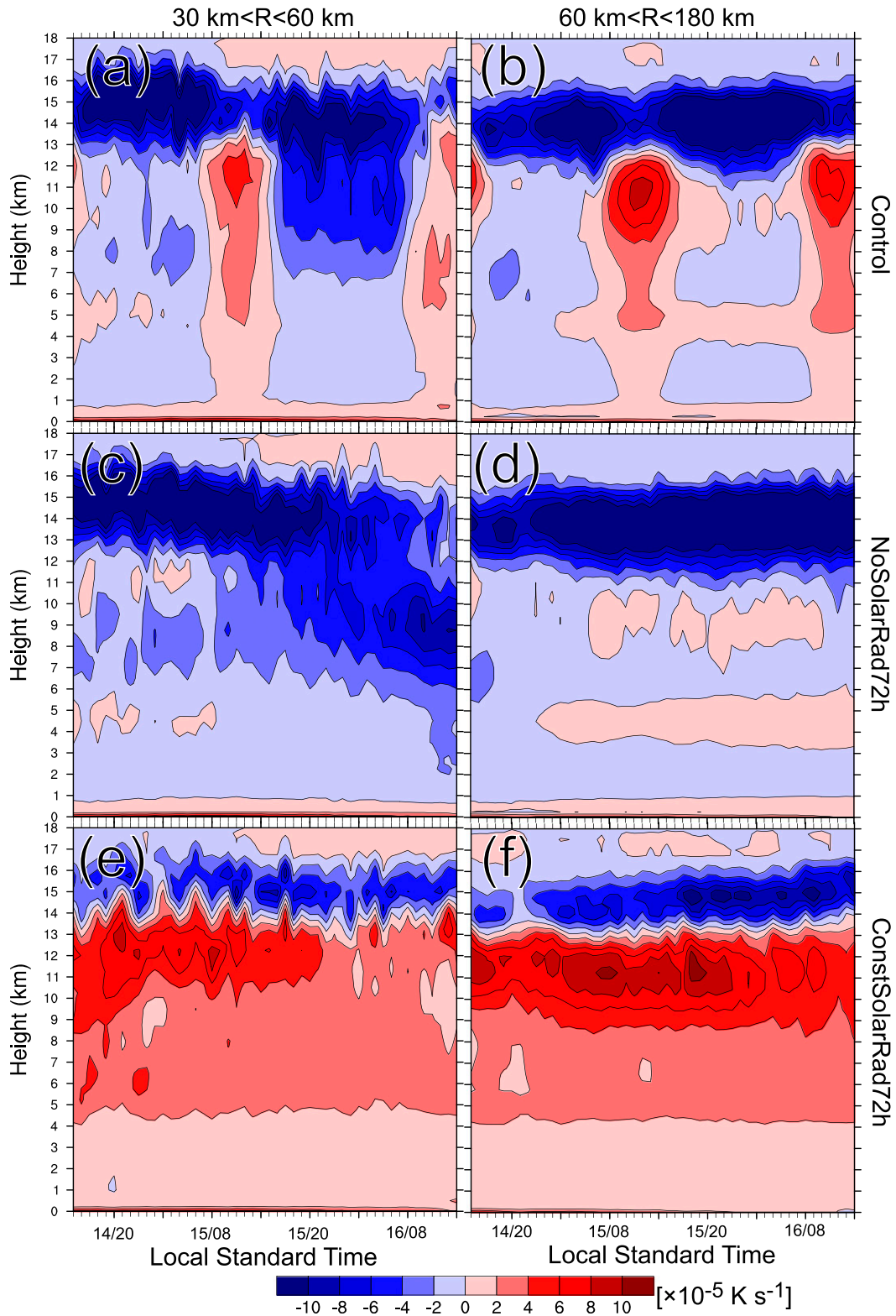


FIG. 11. Vertical profiles of the average net radiation within radial range of (left) 30–60 and (right) 60–180 km for (a),(b) CNTL run and sensitivity experiments (c),(d) NoSolarRad72h and (e),(f) ConstSolarRad72h. The period is from 1900 UTC (1500 LST) 14 Sep to 1800 UTC (1400 LST) 16 Sep.

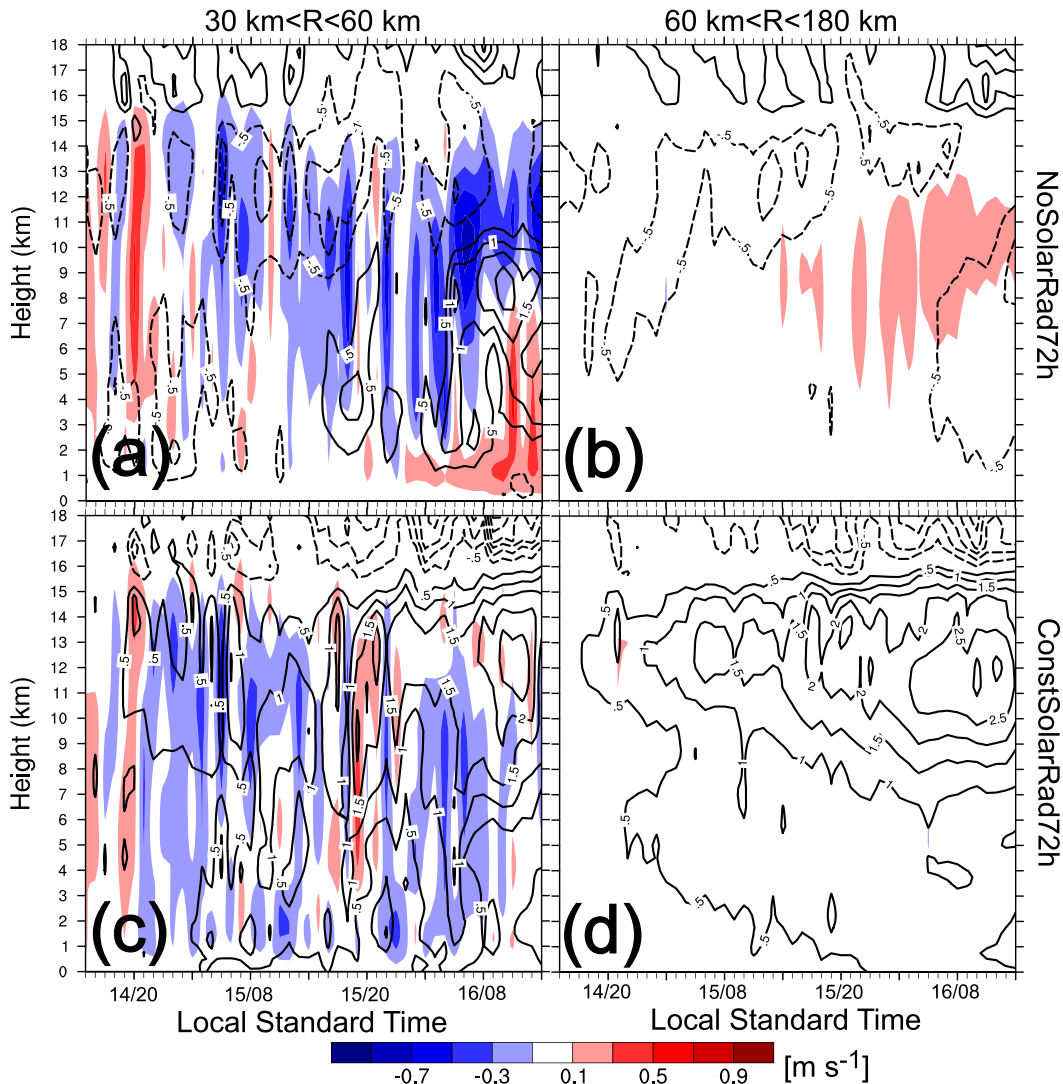


FIG. 12. Vertical profiles of differences of the average vertical velocity (shading) and temperature (contour; solid and dashed denote positive and negative, respectively; zero is omitted; interval is 0.5 K) within radial range of (left) 30–60 and (right) 60–180 km for sensitivity experiments (a),(b) NoSolarRad72h and (c),(d) ConstSolarRad72h minus CNTL run. The period is as in Fig. 11.

maximum difference of 3 K at 11–13-km height (Fig. 12d), and it is lower in NoSolarRad72h with the maximum difference of 1 K (Fig. 12b). The destabilization in the outer-core region can promote deep moist convection in the NoSolarRad72h experiment (Fig. 12b). Similar to the outer core of ConstSolarRad72h, the temperature difference in the 30–60-km radius also has a positive maximum at the height of 10–15 km, causing the decrease of vertical velocity at almost all the time relative to CNTL (Fig. 12c). However, in the region of 30–60-km radius for the NoSolarRad72h experiment, the decreasing vertical velocity is likely due to the expanding eyewall (Fig. 12a). And because of the eyewall expansion with a warmer eye entering

into this region, the temperature difference becomes positive from 2–4 km upward to 9 km gradually from 1900 UTC (1500 LST) 15 September to 1800 UTC (1400 LST) 16 September (Fig. 12a). Figures 13 and 14 also show that the outer-core-averaged vertical velocity is stronger in NoSolarRad72h than CNTL and ConstSolarRad72h, which is even more evident in the mature stage (cf. Figs. 13b,d,f and Figs. 14a,d,g). In NoSolarRad72h, the enhanced outer-core updrafts are mainly composed of vertical velocity of  $1\text{--}2\text{ m s}^{-1}$  at the layer of 6–12 km, while the decreased downdrafts at the same layer also contribute to the greater average upward motion (cf. Figs. 14c,f,i). Enhanced moist convection also induces more release of latent heat, which will further

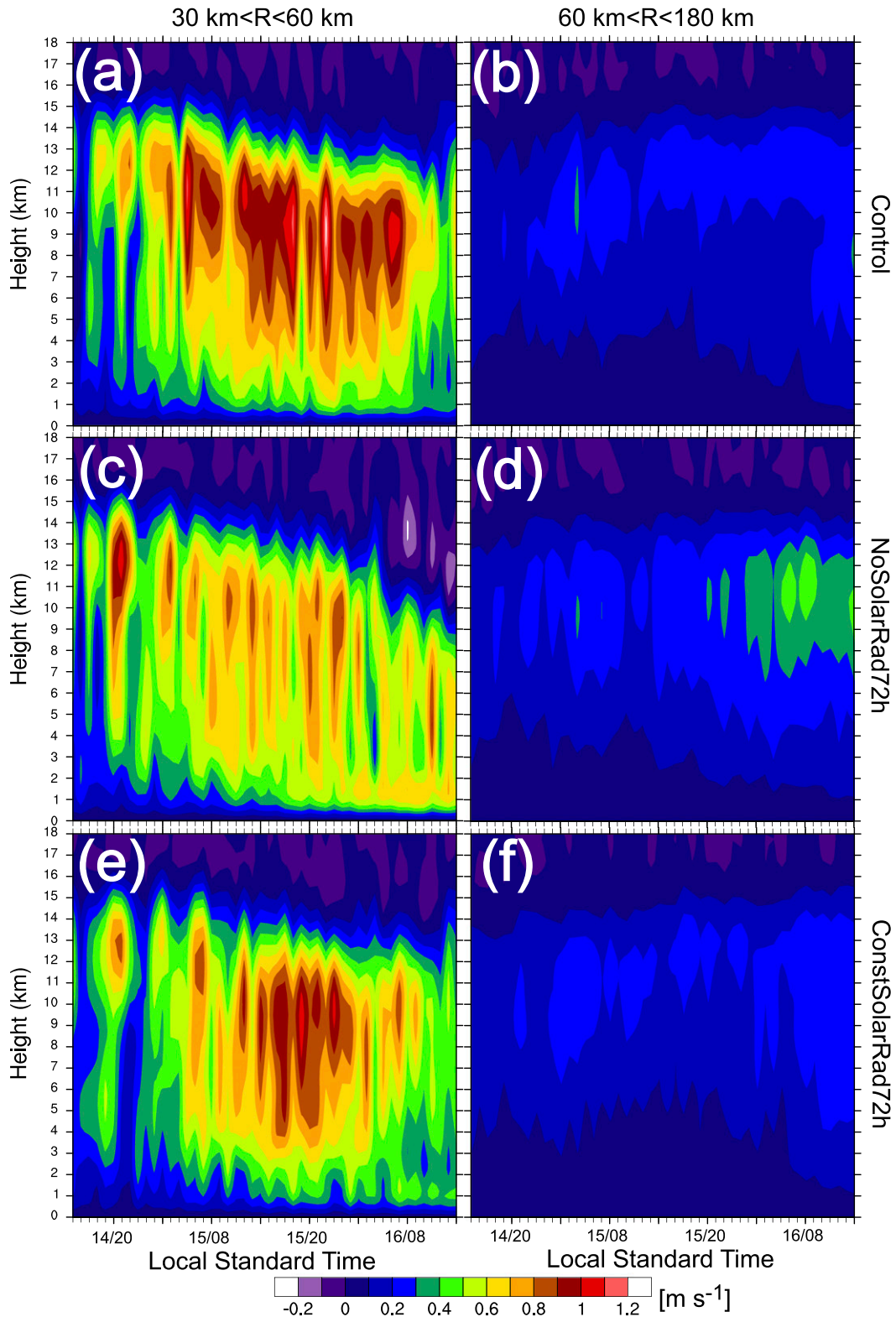


FIG. 13. As in Fig. 11, but for the vertical velocity.

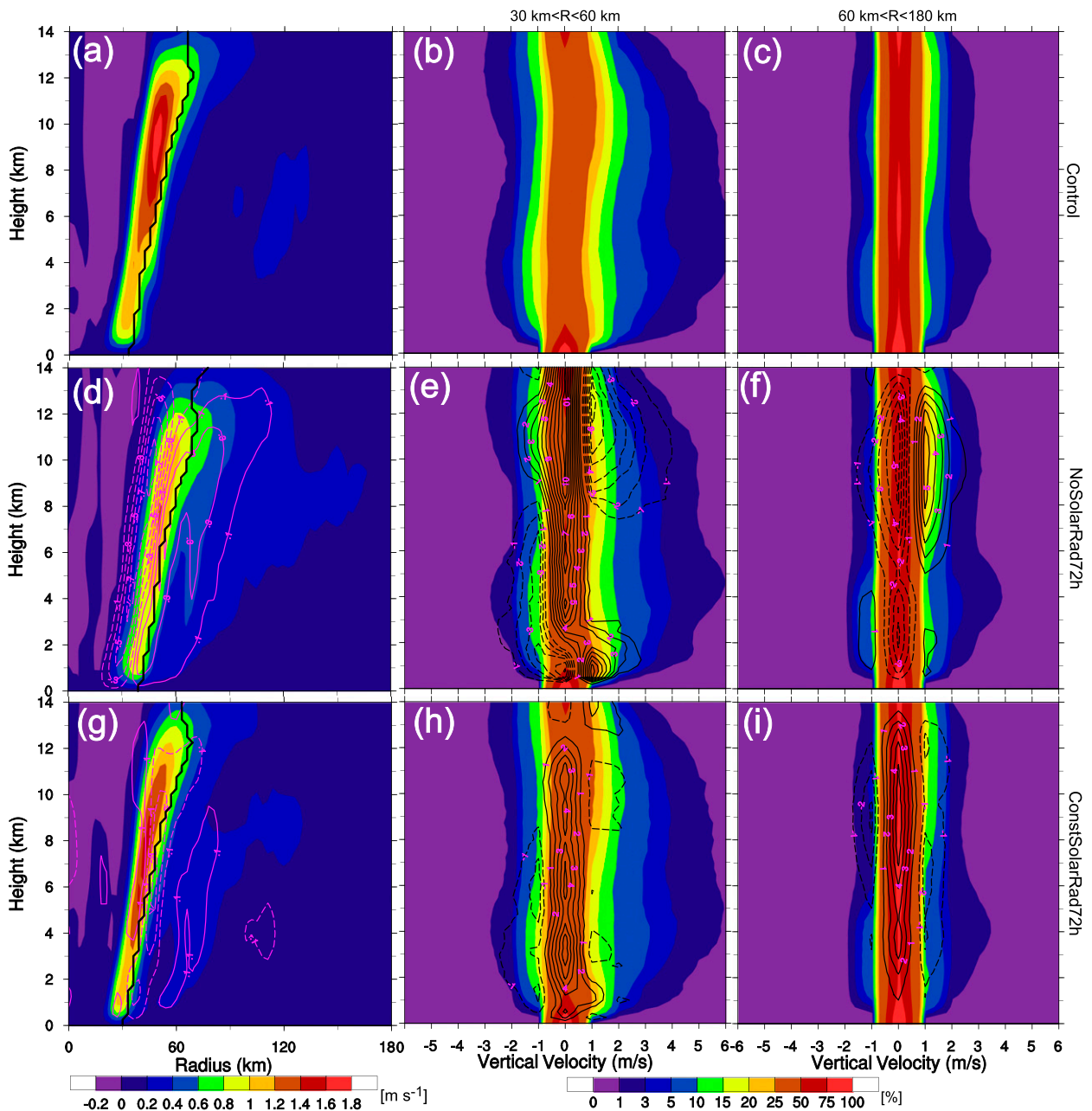


FIG. 14. (left) The 24-h-average azimuth-mean vertical cross sections of vertical velocity from 1900 UTC 15 Sep to 1800 UTC 16 Sep. Contoured mean frequency by altitude diagrams for vertical velocity within radial range of (center) 30–60 and (right) 60–180 km for (a)–(c) CNTL run and sensitivity experiments (d)–(f) NoSolarRad72h and (g)–(i) ConstSolarRad72h. The mean frequency is obtained by averaging the frequency in the 24-h period. Contours are the differences of sensitivity experiments minus the CNTL run (solid and dashed denotes positive and negative, respectively; zero is omitted; contour intervals are  $0.2 \text{ m s}^{-1}$  for left column and 1% for right two columns). Superposed black lines denote RMW in the three leftmost panels.

strengthen the transverse circulation outside the eyewall, resulting in its expansion (cf. Figs. 14a,d,g). Compared with ConstSolarRad72h and CNTL, the average vertical upward motion decreases at the mid- to upper troposphere in the area of 30–60-km radius in NoSolarRad72h with the eyewall expanding from 1900 UTC (1500 LST)

15 September to 1800 UTC (1400 LST) 16 September (Figs. 13a,c,e and Fig. 14d), which results in the decreased updraft mainly of vertical velocity of  $1\text{--}3 \text{ m s}^{-1}$  above the 8-km height (cf. Figs. 14b,e,h). A caveat is that the RMW is shifted outward in NoSolarRad72h, which contributes to some of the differences with CNTL in

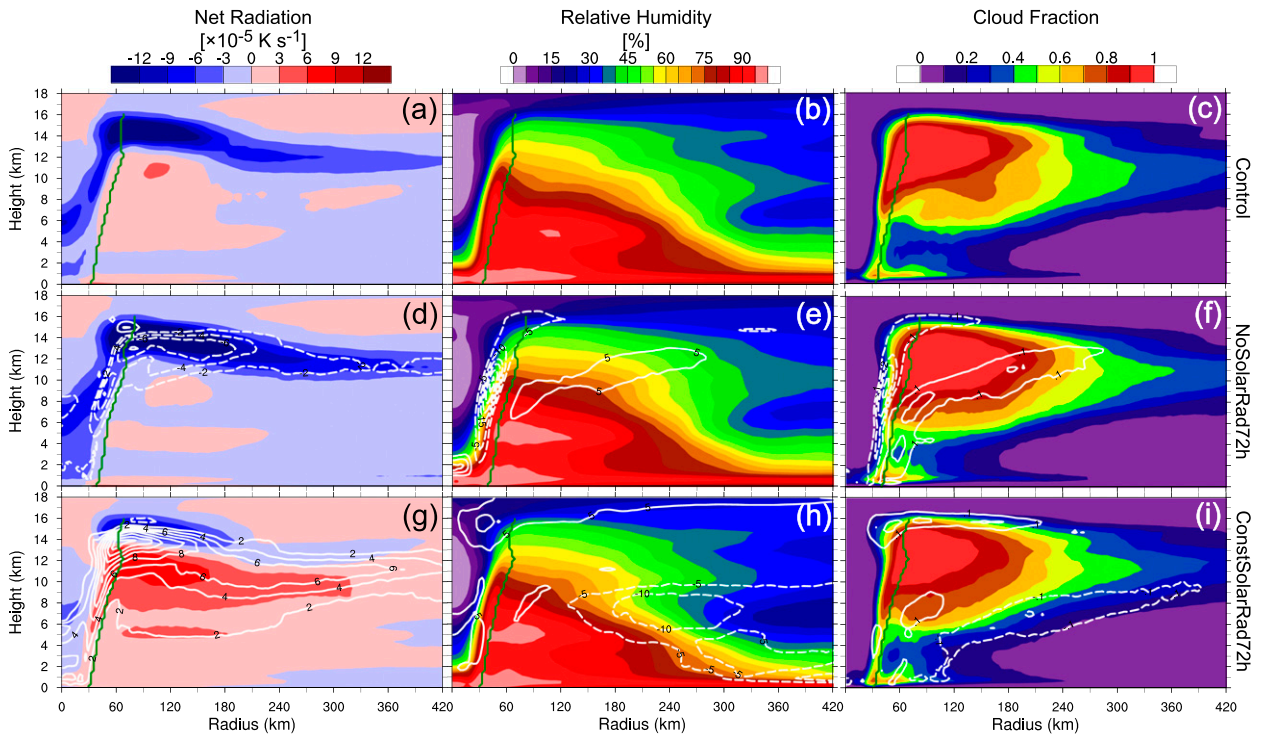


FIG. 15. The 24-h-average azimuth-mean vertical cross sections of (left) net radiation ( $2 \times 10^{-5} \text{ K s}^{-1}$  interval), (center) relative humidity (5% interval), and (right) cloud fraction (0.1 interval) for experiments of (a)–(c) CNTL, (d)–(f) NoSolarRad72h, and (g)–(i) ConstSolarRad72h from 1900 UTC 15 Sep to 1800 UTC 16 Sep. Contours are the differences of sensitivity experiments minus CNTL run (solid and dashed denotes positive and negative, respectively; zero is omitted). Superposed green lines denote RMW at levels of 0–16 km for each panel.

Figs. 14d–f. For example, the decreasing updrafts are along the inner edge of the RMW (Fig. 14d), the weaker upper-level updrafts in NoSolarRad72h are in the 30–60-km radius, and more of the moderate upper-level downdrafts are in the 8–12-km layer (Fig. 14e). These are partly because of compensating subsidence along the inner edge of the eyewall in the 30–60-km radius. The convective activities nearby the RMW are suppressed in ConstSolarRad72h (Fig. 14g). However, on either side of the suppression, the vertical velocity has a slight compensatory increase in ConstSolarRad72h relative to CNTL (Figs. 14g–i), and the overall updrafts are also generally weaker at all times (cf. Figs. 13a,b,e,f). Outside of the 180-km radius, the amplitudes of temperature difference between sensitivity experiments and control run are mostly similar to those at the inner core, but the induced vertical velocity differences are smaller than  $0.1 \text{ m s}^{-1}$  (figures not shown).

c. Impact of radiation on hurricane structure

Figure 15 shows the temporally and azimuthally averaged radiative forcing, latent heating, kinematic field, moisture, and cloud fraction in the radius–height plane from 1900 UTC 15 September to 1800 UTC 16 September;

also shown are the corresponding differences between sensitivity experiments and CNTL. Radiative forcing for CNTL shows strong cooling along the cloud tops, with warming within the cloud due to role of the ice-phase hydrometeors (i.e., cloud ice, snow, and graupel) at higher levels (see Figs. 16a–f), largest within the 60–120-km radius (Fig. 15a). In NoSolarRad72h, cloud-top radiative cooling persists and is stronger than in CNTL, with little within-cloud warming because of the lack of solar short-wave heating (Fig. 15d). Because of artificially enhanced persistent solar radiative heating, the within-cloud radiative warming is much larger in ConstSolarRad72h than both CNTL and NoSolarRad72h (Fig. 15g). The cloud-top cooling in ConstSolarRad72h is also weaker as a result of lesser vigorous convection while the air at middle levels between the 180- and 300-km radii is drier with less cloud ice and snow in ConstSolarRad72h than CNTL (Figs. 15h and 16m,n,o,r) as a result of warming induced by radiative forcing. The maximum differences of relative humidity and all hydrometeors between NoSolarRad72h and CNTL exist inside of the RMW (Fig. 15e and Figs. 16g–l), since the eyewall expansion causes them to decrease substantially in the previous maximum updraft (Fig. 14d).

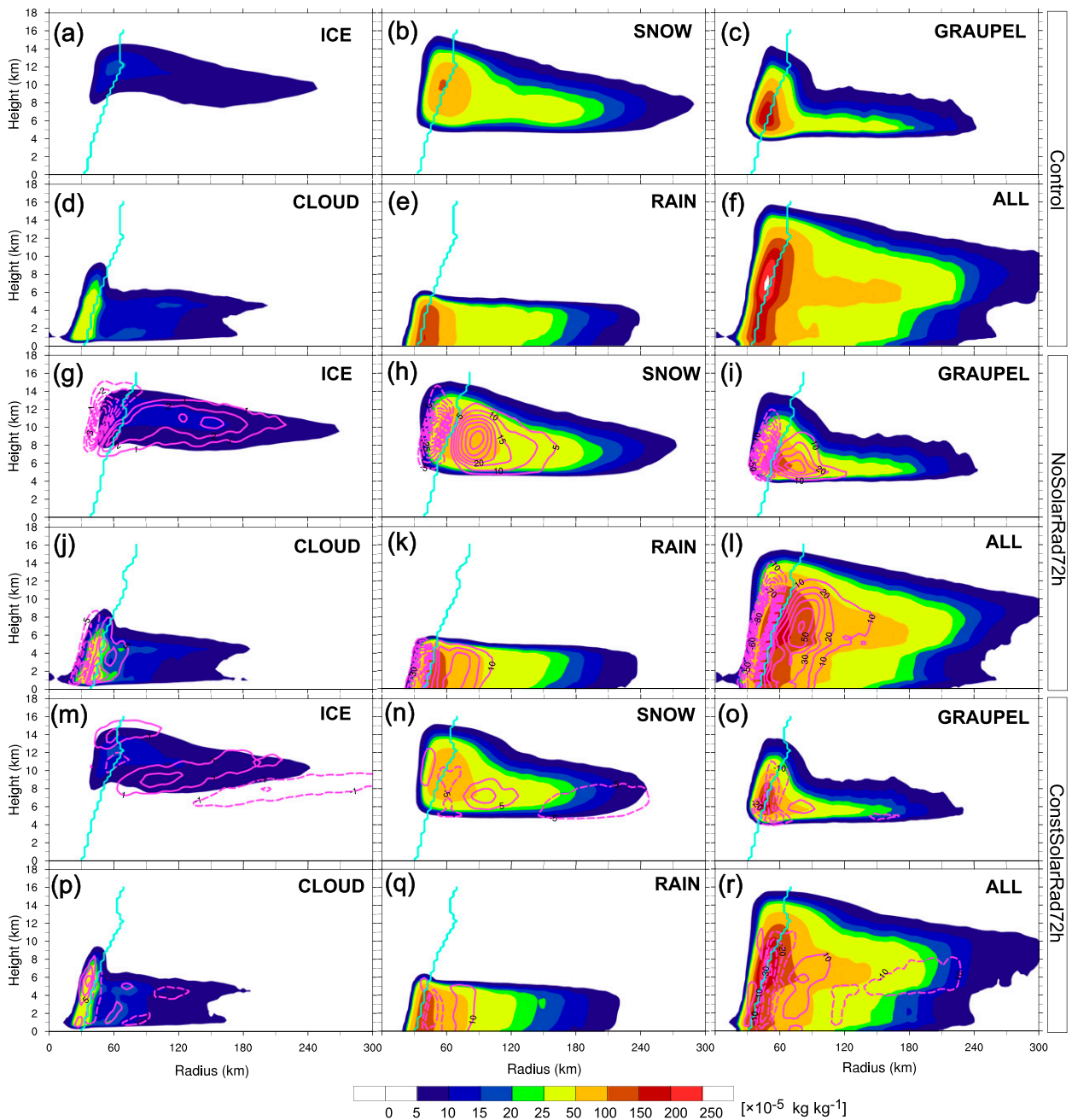


FIG. 16. As in Fig. 15, but for the hydrometeor mixing ratios of ice, snow, graupel, cloud water, rain, and sum of them ( $10^{-5} \text{ kg kg}^{-1}$ ; contour intervals are 1, 5, 10, 5, 10, and  $10 \times 10^{-5} \text{ kg kg}^{-1}$ , respectively) for (a)–(f) CNTL, (g)–(l) NoSolarRad72h, and (m)–(r) ConstSolarRad72h. Superposed cyan lines denote RMW at levels of 0–16 km for each panel.

Two distinct regions of enhanced cloud content, separated by the melting level (roughly 5 km MSL), can be seen in the azimuthally averaged cloud fraction field (Figs. 15c,f,i) and the total hydrometeor mixing ratio (Figs. 16f,l,r) in all three experiments. The NoSolarRad72h storm has the thickest, most radially extensive and outward-sloped cloud shield (Figs. 15f and 16g–i,l), which is associated with

strongest low-level inflow, upper-level outflow, and widest eyewall updraft with latent heating (Figs. 14d and 17c). The largest RMW throughout the troposphere can also be found in NoSolarRad72h storm (Figs. 14d, 15, and 17), which accompanies the expanding eyewall and outer-core strengthening (Figs. 9 and 17d) resulting from the most active convection outside of RMW and in the outer core

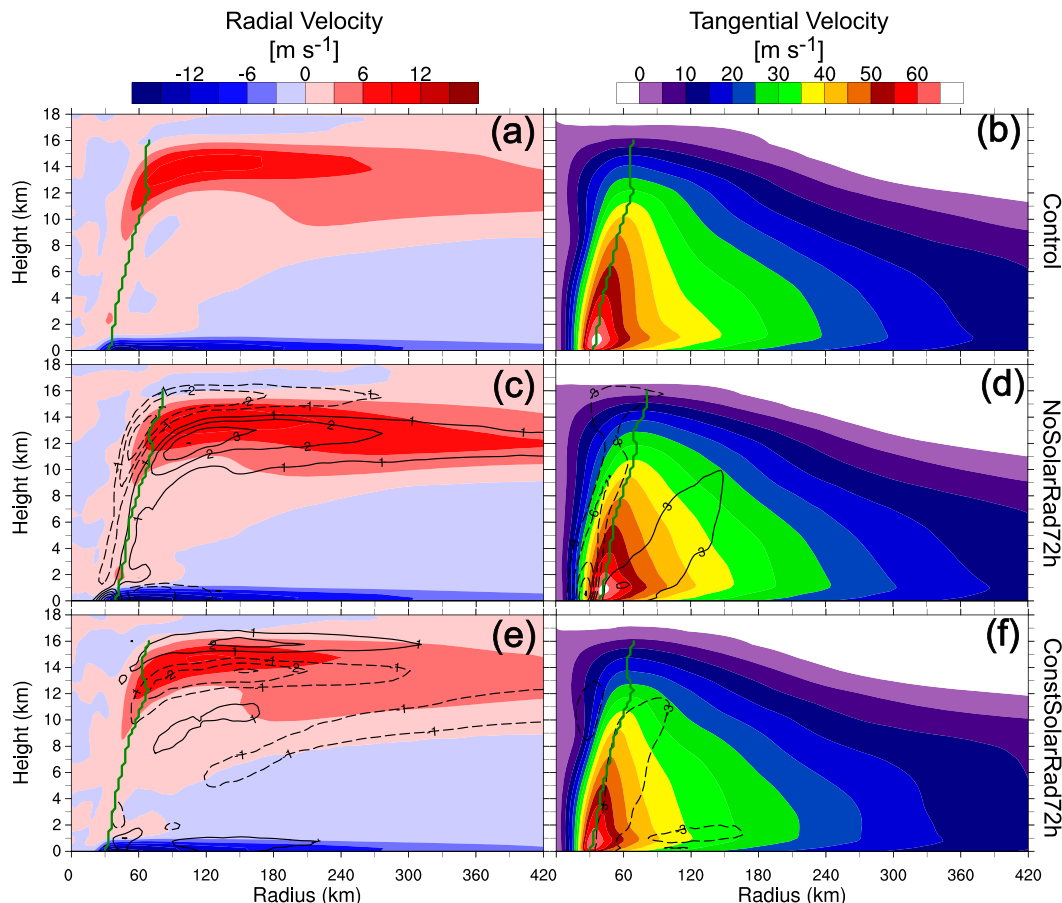


FIG. 17. As in Fig. 15, but for (a),(c),(e) radial velocity ( $1 \text{ m s}^{-1}$  interval) and (b),(d),(f) tangential velocity ( $3 \text{ m s}^{-1}$  interval).

(Figs. 14d,f). The eyewall expansion can be attributed to increased heating outside the RMW and a larger outward tilt of the eyewall. Surface pressure change due to heating resulting mainly from hydrostatic adjustment in the rainbands is significant on the inward side of the rainbands where the inertial stability is generally high, which lowers the surface pressure and increases pressure gradient outside the RMW, thus increasing the inner-core size of the hurricane, consistent with Wang (2009). Heating in the outwardly tilted eyewall, outside the RMW in the mid-troposphere, will increase (reduce) low-level tangential wind outside (near and inside) the RMW that leads to the outward expansion of the RMW while prevents the inward contraction of the RMW (Shapiro and Willoughby 1982). Conversely, the ConstSolarRad72h storm has the smallest RMW and least active convection nearby the RMW and in the outer core (Figs. 9a, 14g-i, and 17e,f). The suppression of updraft nearby the RMW and the slightly increased compensatory updraft on both sides also cause the wavelike radial structure of the hydrometeor mixing ratio (i.e., positive and negative differences

alternately in Figs. 16m-r), which is probably related to the formation of a narrower moat in ConstSolarRad72h (Figs. 8c and 10c).

The structural differences between storms of NoSolarRad96h and ConstSolarRad96h are similar to those of NoSolarRad72h and ConstSolarRad72h (not shown). In closing, after the start of RI, the persistent nighttime phase without solar shortwave heating leads to enhanced convective activities outside of the primary eyewall, leading to the storm broadening and strengthening during the mature stage, although its impacts on the storm's intensity in terms of maximum 10-m wind speed (Fig. 1b) or minimum sea level pressure (Fig. 1d) is rather limited.

### 6. Concluding remarks

High-resolution convection-permitting full-physics simulations with the WRF are used to examine the effects of the diurnal radiation cycle on storm intensification and structure in the formation, rapid

intensification, and mature stages of Hurricane Edouard (2014). Sensitivity experiments with either endless daytime (persistent maximum solar shortwave forcing) or endless nighttime (no solar radiative forcing) applied at different model integration periods are designed to isolate the varying roles of the diurnal radiation cycle during different stages of the storm's life cycle. These results show the influences of the diurnal radiation variation on storms and related processes are significantly different among stages from its formation to maturity.

In the formation stages of tropical cyclones, the sensitivity to the heating and cooling associated with the diurnal cycle is mainly on the intensification rate. The nighttime phase of the diurnal radiation cycle provides radiative cooling in the local and large-scale environment, which leads to an increase in humidity and decrease in stability, both of which favor deep moist convection and improve the potential for cyclogenesis. The greater latent heating released by deep convection induces stronger low-level inflow, which results in convergence of absolute vorticity and increase of low-level cyclonic winds (Fang and Zhang 2010). In the meantime, the RMW contracts inwards substantially to form a compact and well-organized storm. On the contrary, the daytime-phase radiation reduces relative humidity and increases stability, which is less favorable for deep moist convection and storm development. Consequently, solar radiation has a suppressing role for TC genesis and early development. The impact of the diurnal radiation cycle on TC genesis is similar to the findings of Melhauser and Zhang (2014) on their study of Hurricane Karl (2010). Moreover, the large track difference between a poorly developed disturbance in the experiment with constant and excessive solar shortwave radiation and the control run could be due to differences in the effective steering layer, tied to the storm intensity (Velden and Leslie 1991) and/or due to the beta drift effect (Holland 1983; Fang and Zhang 2012; Qian et al. 2013). These reveal that the effect of the diurnal radiation cycle is very critical to the storm intensification rate and even the track in the formation stages.

Once the storm commences rapid intensification and then becomes mature, the diurnal radiation cycle mainly impacts the storm structure and strength (rather than track and intensity). The large-scale cooling in the nighttime phase increases outer-core relative humidity, promoting deep moist convection and more active rainbands outside of the eyewall. The latent heating released by enhanced convection induces stronger low-level inflow outside the eyewall. Hydrostatic adjustment causes surface pressure to lower significantly on the inward side of these rainbands as a result of heating, where the inertial stability is generally high, thus increasing the

pressure gradient outside the RMW and hurricane inner-core size (Wang 2009). The eyewall is most outwardly tilted in the nighttime phase (Figs. 14–17), while heating outside the RMW in the midtroposphere will increase (reduce) low-level tangential wind outside (near and inside) the RMW and lead to the outward expansion of the RMW (Shapiro and Willoughby 1982) and thus a larger and stronger hurricane in the experiment without solar insolation. In the daytime phase of diurnal cycle, the shortwave radiation heating decreases the relative humidity in the outer core, making it less conducive to deep moist convection and thus weaker outer rainbands development.

It seems that the changes in both convective instability and the large-scale nighttime cooling play important roles in all the stages of tropical cyclone development. However, the differential heating mechanism may act together with the other two mainly in the RI and mature stages of the storm when it has a well-organized eyewall and thicker and broader cloud canopy. It is also found that the impact of radiation is an integrated effect, taking at least about half a day to noticeably alter the environment for the modifications and subsequently the storm in the sensitivity experiments, as is also shown in Melhauser and Zhang (2014). In the control simulation, there is no obvious diurnal change in storm size during the mature stage likely as a result of an integrated effect in the switch-on or -off of shortwave radiation forcing between day and night. Under the long-time integrated effect of nighttime cooling of the environment, the final strength of the storms in experiments without solar insolation are greater than those in the corresponding experiments with constant solar insolation, though the occurrence may be later than in the control run. However, the difference of radiation between the daytime and nighttime phase has only a minor and inconsistent impact on the maximum tangential wind during the mature phase.

Another interesting finding is that there is a distinct secondary eyewall formation in the control simulation with a normal diurnal radiation cycle that has a strong resemblance to the observed storm (Stewart 2014), while no secondary eyewall forms in the experiments without solar insolation (while a narrower moat is in the experiments with constant solar insolation during the eyewall replacement cycle). There is less convective activity and less-developed outer rainbands in the experiments with constant solar insolation such that the secondary eyewall tends to form at a smaller radius in the drier (lower relative humidity) environment. However, the absence of secondary eyewall formation in the experiments without solar radiation may be caused by the outward expansion of the primary eyewall, which

prohibits moat formation (cf. Terwey and Montgomery 2008; Fang and Zhang 2012). Both outer and inner rainbands were active but they were too close to each other for moat formation. The interaction between inner rainbands and eyewall convection could lead to the formation of annular hurricane with a wider eyewall and a larger eye, as is also shown in Wang (2008). Nevertheless, the detailed impacts of radiation to SEF and subsequent eyewall replacement cycle and underlying dynamics are under investigation and will be reported elsewhere when completed. Future work is also planned to test how these results depend on different representation of cloud–radiative processes using other pairings of radiation schemes and microphysics schemes.

*Acknowledgments.* The research was conducted during the first author's sabbatical visit at The Pennsylvania State University. The authors thank Yonghui Weng for performing the real-time ensemble data assimilation and Erin B. Munsell and Christopher Melhauser for performing the control run and sensitivity experiments. We benefited greatly from interactions with Jason Dunion, whose blog post at the tropical storm list on the observed diurnal cycle of Edouard inspired us to examine its evolution and impacts in this event through numerical sensitivity experiments. We also benefited from discussions with Christopher Melhauser, Chris Velden, Chris Davis, Robert Rogers, Zhe-Min Tan, and others. Review comments from Chris Velden and an anonymous reviewer were very beneficial. This work was supported by National Nature Science Foundation of China (Grants 41275056, 41461164008, and 41130964), State Scholarship Fund by China Scholarship Council, and a project funded by the Priority Academic Program Development (PAPD) of Jiangsu Higher Education Institutions. FZ was partially supported by ONR Grant N000140910526 and NOAA Hurricane Forecast Improvement Project (HFIP). Computing at the Texas Advanced Computing Center (TACC) and NOAA Jet clusters at the Earth System Research Laboratory (ESRL) is acknowledged.

#### REFERENCES

- Barker, D. M., W. Huang, Y.-R. Guo, A. J. Bourgeois, and Q. N. Xiao, 2004: A three-dimensional variational data assimilation system for MM5: Implementation and initial results. *Mon. Wea. Rev.*, **132**, 897–914, doi:10.1175/1520-0493(2004)132<0897:ATVDAS>2.0.CO;2.
- Browner, S. P., W. L. Woodley, and C. G. Griffith, 1977: Diurnal oscillation of the area of cloudiness associated with tropical storms. *Mon. Wea. Rev.*, **105**, 856–864, doi:10.1175/1520-0493(1977)105<0856:DOOTAO>2.0.CO;2.
- Bu, Y. P., R. G. Fovell, and K. L. Corbosiero, 2014: Influence of cloud–radiative forcing on tropical cyclone structure. *J. Atmos. Sci.*, **71**, 1644–1662, doi:10.1175/JAS-D-13-0265.1.
- Craig, G., 1996: Numerical experiments on radiation and tropical cyclones. *Quart. J. Roy. Meteor. Soc.*, **122**, 415–422, doi:10.1002/qj.49712253006.
- Dudhia, J., 1989: Numerical study of convection observed during the Winter Monsoon Experiment using a mesoscale two-dimensional model. *J. Atmos. Sci.*, **46**, 3077–3107, doi:10.1175/1520-0469(1989)046<3077:NSOCOD>2.0.CO;2.
- Dunion, J. P., C. D. Thorncroft, and C. S. Velden, 2014: The tropical cyclone diurnal cycle of mature hurricanes. *Mon. Wea. Rev.*, **142**, 3900–3919, doi:10.1175/MWR-D-13-00191.1.
- Fang, J., and F. Zhang, 2010: Initial development and genesis of Hurricane Dolly (2008). *J. Atmos. Sci.*, **67**, 655–672, doi:10.1175/2009JAS3115.1.
- , and —, 2012: Effect of beta shear on simulated tropical cyclones. *Mon. Wea. Rev.*, **140**, 3327–3346, doi:10.1175/MWR-D-10-05021.1.
- Gray, W. M., and R. W. Jacobson Jr., 1977: Diurnal variation of deep cumulus convection. *Mon. Wea. Rev.*, **105**, 1171–1188, doi:10.1175/1520-0493(1977)105<1171:DVODCC>2.0.CO;2.
- Grell, G. A., and S. R. Freitas, 2014: A scale and aerosol aware stochastic convective parameterization for weather and air quality modeling. *Atmos. Chem. Phys.*, **14**, 5233–5250, doi:10.5194/acp-14-5233-2014.
- Hobgood, J. S., 1986: A possible mechanism for the diurnal oscillations of tropical cyclones. *J. Atmos. Sci.*, **43**, 2901–2922, doi:10.1175/1520-0469(1986)043<2901:APMFTD>2.0.CO;2.
- Holland, G. J., 1983: Tropical cyclone motion: Environmental interaction plus a beta effect. *J. Atmos. Sci.*, **40**, 328–342, doi:10.1175/1520-0469(1983)040<0328:TCMEIP>2.0.CO;2.
- , and R. T. Merrill, 1984: On the dynamics of tropical cyclone structural changes. *Quart. J. Roy. Meteor. Soc.*, **110**, 723–745, doi:10.1002/qj.49711046510.
- Hong, S., and J. J. Lim, 2006: The WRF single-moment 6-class microphysics scheme (WSM6). *J. Korean Meteor. Soc.*, **42**, 129–151.
- , Y. Noh, and J. B. Dudhia, 2006: A new vertical diffusion package with an explicit treatment of entrainment processes. *Mon. Wea. Rev.*, **134**, 2318–2341, doi:10.1175/MWR3199.1.
- Johnson, R. H., T. M. Rickenbach, S. A. Rutledge, P. E. Ciesielski, and W. H. Schubert, 1999: Trimodal characteristics of tropical convection. *J. Climate*, **12**, 2397–2418, doi:10.1175/1520-0442(1999)012<2397:TCOTC>2.0.CO;2.
- Kossin, J. P., 2002: Daily hurricane variability inferred from GOES infrared imagery. *Mon. Wea. Rev.*, **130**, 2260–2270, doi:10.1175/1520-0493(2002)130<2260:DHVIFG>2.0.CO;2.
- Lajoie, F. A., and I. J. Butterworth, 1984: Oscillation of high-level cirrus and heavy precipitation around Australian region tropical cyclones. *Mon. Wea. Rev.*, **112**, 535–544, doi:10.1175/1520-0493(1984)112<0535:OOHLCA>2.0.CO;2.
- Maclay, K. S., M. Demaria, and T. H. V. Haar, 2008: Tropical cyclone inner-core kinetic energy evolution. *Mon. Wea. Rev.*, **136**, 4882–4898, doi:10.1175/2008MWR2268.1.
- Marchok, T. P., 2002: How the NCEP tropical cyclone tracker works. Preprints, *25th Conf. on Hurricanes and Tropical Meteorology*, San Diego, CA, Amer. Meteor. Soc., P1.13. [Available online at [https://ams.confex.com/ams/25HURR/techprogram/paper\\_37628.htm](https://ams.confex.com/ams/25HURR/techprogram/paper_37628.htm).]
- Melhauser, C., and F. Zhang, 2014: Diurnal radiation cycle impact on the pregenesis environment of Hurricane Karl (2010). *J. Atmos. Sci.*, **71**, 1241–1259, doi:10.1175/JAS-D-13-0116.1.
- Mlawer, E. J., S. J. Taubman, P. D. Brown, M. J. Iacono, and S. A. Clough, 1997: Radiative transfer for inhomogeneous atmosphere: RRTM, a validated correlated-k model for the

- long-wave. *J. Geophys. Res.*, **102**, 16663–16682, doi:10.1029/97JD00237.
- Muramatsu, T., 1983: Diurnal variations of satellite-measured TBB areal distribution and eye diameter of mature typhoons. *J. Meteor. Soc. Japan*, **61**, 77–89.
- Nicholls, M. E., 2015: An investigation of how radiation may cause accelerated rates of tropical cyclogenesis and diurnal cycles of convective activity. *Atmos. Chem. Phys.*, **15**, 9003–9029, doi:10.5194/acp-15-9003-2015.
- Qian, C., F. Zhang, B. W. Green, J. Zhang, and X. Zhou, 2013: Probabilistic evaluation of the dynamics and prediction of Supertyphoon Megi (2010). *Wea. Forecasting*, **28**, 1562–1577, doi:10.1175/WAF-D-12-00121.1.
- Shapiro, L. J., and H. E. Willoughby, 1982: The response of balanced hurricanes to local sources of heat and momentum. *J. Atmos. Sci.*, **39**, 378–394, doi:10.1175/1520-0469(1982)039<0378:TROBHT>2.0.CO;2.
- Shu, H.-L., Q.-H. Zhang, and B. Xu, 2013: Diurnal variation of tropical cyclone rainfall in the western north Pacific in 2008–2010. *Atmos. Oceanic Sci. Lett.*, **6**, 103–108, doi:10.1080/16742834.2013.11447064.
- Skamarock, W. C., and Coauthors, 2008: A description of the Advanced Research WRF version 3. NCAR Tech. Note NCAR/TN-475+STR, 113 pp., doi:10.5065/D68S4MVH.
- Steranka, J., E. B. Rodgers, and R. C. Gentry, 1984: The diurnal variation of Atlantic Ocean tropical cyclone cloud distribution inferred from geostationary satellite infrared measurements. *Mon. Wea. Rev.*, **112**, 2338–2344, doi:10.1175/1520-0493(1984)112<2338:TDOVAO>2.0.CO;2.
- Stewart, S. R., 2014: Hurricane Edouard (AL062014), 11–19 September 2014. National Hurricane Center Tropical Cyclone Rep., 19 pp. [Available online at [http://www.nhc.noaa.gov/data/tcr/AL062014\\_Edouard.pdf](http://www.nhc.noaa.gov/data/tcr/AL062014_Edouard.pdf).]
- Tallapragada, V., and Coauthors, 2013: Hurricane Weather Research and Forecasting (HWRF) model: 2013 scientific documentation. Developmental Testbed Center, 99 pp. [Available online at [http://www.dtcenter.org/HurrWRF/users/docs/scientific\\_documents/HWRFv3.5a\\_ScientificDoc.pdf](http://www.dtcenter.org/HurrWRF/users/docs/scientific_documents/HWRFv3.5a_ScientificDoc.pdf).]
- Tao, W.-K., J. Simpson, S. Lang, C.-H. Sui, B. Ferrier, and M.-D. Chou, 1996: Mechanisms of cloud–radiation interaction in the tropics and midlatitudes. *J. Atmos. Sci.*, **53**, 2624–2651, doi:10.1175/1520-0469(1996)053<2624:MOCRII>2.0.CO;2.
- Terwey, W. D., and M. T. Montgomery, 2008: Secondary eyewall formation in two idealized, full-physics modeled hurricanes. *J. Geophys. Res.*, **113**, 1984–2012, doi:10.1029/2007JD008897.
- Velden, C. S., and L. M. Leslie, 1991: The basic relationship between tropical cyclone intensity and the depth of the environmental steering layer in the Australian region. *Wea. Forecasting*, **6**, 244–253, doi:10.1175/1520-0434(1991)006<0244:TBRBTC>2.0.CO;2.
- Wang, Y., 2008: Structure and formation of an annular hurricane simulated in a fully compressible, nonhydrostatic model—TCM4. *J. Atmos. Sci.*, **65**, 1505–1527, doi:10.1175/2007JAS2528.1.
- , 2009: How do outer spiral rainbands affect tropical cyclone structure and intensity? *J. Atmos. Sci.*, **66**, 1250–1273, doi:10.1175/2008JAS2737.1.
- Webster, P. J., and G. L. Stephens, 1980: Tropical upper-tropospheric extended clouds: Inference from winter MONEX. *J. Atmos. Sci.*, **37**, 1521–1541, doi:10.1175/1520-0469-37.7.1521.
- Weng, Y., and F. Zhang, 2016: Advances in convection-permitting tropical cyclone analysis and prediction through EnKF assimilation of reconnaissance aircraft observations. *J. Meteor. Soc. Japan*, doi:10.2151/jmsj.2016-018, in press.
- Wu, Q., Z. Ruan, D. Chen, and T. Lian, 2015: Diurnal variations of tropical cyclone precipitation in the inner and outer rainbands. *J. Geophys. Res. Atmos.*, **120**, 1–11, doi:10.1002/2014JD022190.
- Xu, J., and Y. Wang, 2010: Sensitivity of tropical cyclone inner-core size and intensity to the radial distribution of surface entropy flux. *J. Atmos. Sci.*, **67**, 1831–1852, doi:10.1175/2010JAS3387.1.
- Xu, K.-M., and D. A. Randall, 1995: Impact of interactive radiative transfer on the macroscopic behavior of cumulus ensembles. Part II: Mechanisms for cloud–radiation interactions. *J. Atmos. Sci.*, **52**, 800–817, doi:10.1175/1520-0469(1995)052<0800:IOIRTO>2.0.CO;2.
- Yaroshevich, M. I., and L. Kh. Ingel, 2013: Diurnal variations in the intensity of tropical cyclones. *Izv., Atmos. Ocean. Phys.*, **49**, 375–379, doi:10.1134/S0001433813040117.
- Zhang, F., and Y. Weng, 2015: Predicting hurricane intensity and associated hazards: A five-year real-time forecast experiment with assimilation of airborne Doppler radar observations. *Bull. Amer. Meteor. Soc.*, **96**, 25–33, doi:10.1175/BAMS-D-13-00231.1.